

# Space-time formulation, discretization, and computational performance studies for phase-field fracture optimal control problems

D. Khimin<sup>1</sup>, M. C. Steinbach<sup>1</sup>, and T. Wick<sup>1,2</sup>

<sup>1</sup>Leibniz Universität Hannover, Institut für Angewandte Mathematik, Welfengarten 1, 30167 Hannover, Germany

<sup>2</sup>Université Paris-Saclay, ENS Paris-Saclay, LMT – Laboratoire de Mécanique et Technologie, 91190 Gif-sur-Yvette, France

September 7, 2022

## Abstract

The purpose of this work is the development of space-time discretization schemes for phase-field optimal control problems. Specifically in the optimal control minimization problem, a tracking-type cost functional is minimized to steer the crack via the phase-field variable into a desired pattern. To achieve such optimal solutions, Neumann type boundary conditions need to be determined. First, a time discretization of the forward problem is derived using a discontinuous Galerkin formulation. Here, a challenge is to include regularization terms and the crack irreversibility constraint. The optimal control setting is formulated by means of the Lagrangian approach from which the primal part, adjoint, tangent and adjoint Hessian are derived. Herein the overall Newton algorithm is based on a reduced approach by eliminating the state constraint, namely the displacement and phase-field unknowns, but keeping the control variable as the only unknown. From the low-order discontinuous Galerkin discretization, adjoint time-stepping schemes are finally obtained. Both our formulation and algorithmic developments are substantiated and illustrated with six numerical experiments.

## Keywords:

Space-time, phase-field fracture, optimal control, reduced optimization approach, Galerkin discretization

## AMS:

74R10, 65N30, 49M15, 49K20, 35Q74

## 1 Introduction

Fracture propagation using variational approaches and phase-field methods is currently an important topic in applied mathematics and engineering. The approach for the mathematical and mechanical

literature was established in [25, 13, 40] and in physics by [34, 29, 56] and overview articles and monographs include [14, 15, 63, 61, 24, 22] with numerous further references cited therein.

It is well-known that the efficient and robust numerical solution of the nonlinear and linear sub-problems in phase-field fracture is challenging. This is mainly due to the nonlinear structure of the coupled problem and the interaction of model, discretization and material parameters. In spite of the development of robust preconditioning and parallel, scalable, iterative algorithms, the forward solution remains costly in general for both two-dimensional and three-dimensional settings.

While the major amount of work concentrates on forward modeling of phase-field fracture, more recently some work started on parameter identification employing Bayesian inversion [36, 64, 53, 54], topology optimization [21], stochastic phase-field modeling [27], and optimal control [51, 52, 50]. Solving phase-field fracture problems using methods from shape optimization was proposed in [1].

The main objective of this work is to design a mathematical framework including computational performance studies for phase-field fracture optimal control problems. In optimal control some cost functional shall be minimized where the forward problem (here the phase-field fracture weak formulation) acts as constraint and the control (often involving boundary conditions or right hand side forces) is designed in such a way that the minimization goal is achieved as well as possible. Specifically, we consider a tracking type cost functional in which a desired phase-field crack pattern shall be realized by controlling Neumann type boundary forces. From an engineering viewpoint, such cost functionals and controls are reasonable since often either a desired crack path shall be achieved (for instance in hydraulic fracturing), or in the case of preventing fracture/damage either no fractures should develop or at least once they start developing they should be steered with appropriate forces into directions that cause minimal damage. Since volume forces such as gravitational forces play minor roles in such settings, we mainly control optimal fracture patterns by boundary forces and concentrate on Neumann type conditions. In prior work [51, 52] the emphasis was on mathematical analysis and a brief illustration in terms of a numerical simulation for a fixed fracture by a tracking type functional for a desired displacement field. However, computational details have not yet been discussed therein, but are necessary in order to apply and investigate the methodology for more practical applications such as propagating fractures.

Due to the irreversibility constraint on the fracture growth, optimization problems subject to such an evolution become mathematical programs with complementarity constraints (MPCC) [7, 46, 47] so that standard constraint qualifications like [55, 66] cannot hold. Our computational approach requires stronger regularity and hence we replace the complementarity constraint with a suitable penalty term.

Designing a computational framework for phase-field fracture optimal control is novel and challenging because appropriate function spaces and weak formulations need to be determined, and robust forward and optimization solvers are required.

Specifically, we are interested in a rigorous mathematical framework, which is the reason why we concentrate on one type of cost functional (here tracking type) and one type of controls (here Neumann boundary controls) in this work. However, from an engineering perspective other controls such as Dirichlet controls or right hand side controls would be possible, too. Moreover, other cost

functionals controlling for instance the bulk or crack energies could be employed. Technically, such implementations can be realized in our software as shown for other numerical experiments in [23, 28].

For the forward solver, as intensively discussed in the literature, the linear and nonlinear solutions are demanding because of the non-convexity of the governing energy functional of the forward phase-field fracture model and the relationship of discretization and regularization parameters. For the nonlinear solution various methods were proposed such as alternating minimization (staggered solution) [12, 19], quasi-monolithic solutions [30, 32, 61], and fully monolithic schemes [26, 59, 60, 39, 58]. Nonetheless, monolithic solutions as adopted here remain difficult and we add an additional viscous regularization term as originally proposed in [37] and used in our governing model from [52].

The optimal control problem is formulated in terms of the reduced approach by eliminating the state variable with a control-to-state operator; see for instance [57, 31]. In this work, the state variable consists of the vector-valued displacement field and the phase-field variable. The control variable is a function defined on the boundary of the domain. By eliminating the state variable, we obtain a so-called reduced cost functional defined in terms of the control variable only, which results in an unconstrained optimization problem. The numerical solution is obtained via the first-order necessary optimality condition.

Applying Newton-type methods requires the second derivative of the reduced cost functional, and needs in practice the evaluation of the *adjoint*, *tangent*, and *adjoint Hessian equations*. The latter requires the evaluation of second-order derivatives; see, e.g., [8] and [42, Chapter 4] for parabolic optimization problems.

The paper [8] serves as point of departure for our approach in the current work. Specifically, we employ Galerkin formulations in time and discuss in detail how the crack irreversibility constraint is formulated using a penalization [48, 51] and an additional viscous regularization [52, 37]. Based on these settings, concrete time-stepping schemes are derived. As usual, the primal and tangent problem run forward in time whereas the adjoint and adjoint Hessian equations run backward in time. The main emphasis is to establish robust numerical solvers in terms of the nonlinear forward solver and the nonlinear optimization loop.

We then perform extensive tests by means of six numerical experiments with different complexities. First, we notice that propagating fractures for such optimization problems were not addressed in the prior work [51, 52]. In the current work, considering now propagating fractures, the overall goals are computational investigations of the performance of the reduced Newton algorithm (NLP), the linear conjugate gradient (CG) method, and convergence of the residuals, cost functionals, tracking parts, Tikhonov parts and optimal controls. We recall upfront that such investigations are even challenging for forward phase-field fracture problems due to the interaction of model, discretization and material parameters (see [13, 38] and closely related work on image segmentation [11], and the prior seminal work on Gamma convergence [3, 4, 17]), and possibly also penalization parameters for treating the crack irreversibility constraint [61]. All of them have an impact on mathematical well-posedness [14] (and references cited therein), and on numerical approximations and nonlinear and linear solution algorithms [14, 15, 63, 61, 24, 22]. The parameters include: phase-field regularization  $\varepsilon$  and bulk

regularization  $\kappa$ , crack irreversibility penalization  $\gamma$  and viscous regularization  $\eta$ , mesh size  $h$  and loading step size  $\Delta t$ , critical energy release rate  $G_c$  and Lamé parameters  $\lambda$  and  $\mu$ .

The extension to optimization adds further levels of complexity: the forward problem, with all its own challenges, must be solved numerous times, more parameters enter such as the Tikhonov regularization  $\alpha$ , and in order to guarantee a well-posed optimization setting, the adjustment of  $\alpha$  is delicate for weighting the physical tracking functional against the Tikhonov regularization term. Our experiments below encompass propagating fractures, non-constant controls on one or more boundary sections, multiple (propagating) fractures, an adaptation of Winkler's [62] L-shaped panel test, and using controls to prevent crack growth. These tests provide novel insight for both the capabilities of the phase-field method for fracture from a numerical viewpoint as well as for applications. On the other hand, limitations and opportunities for future work also become visible, such as the need to further improve the linear solver's cost complexity (e.g., by parallel multigrid methods [33] and model order reduction [9]) as for fine meshes the forward solver becomes prohibitively expensive. Some further preliminary results (yet with a stationary, non-propagating fracture) are published in the book chapter [35].

The outline of this paper is as follows: In Section 2, the phase-field fracture forward model is introduced. Furthermore, a Galerkin time discretization is derived. Next, in Section 3, the optimization problem is stated, including the reduced space approach. In the key Section 4, the Lagrangian and three auxiliary equations are carefully derived in great detail, and with our final complete algorithm. Then, in Section 5, extensive studies with six numerical experiments are discussed to substantiate our algorithmic developments. Our work is summarized in Section 6.

## 2 Space-time phase-field fracture forward model

To formulate the space-time forward problem, we first introduce some basic notation and then proceed with the construction of function spaces and a space-time weak formulation. Afterwards, a space-time Galerkin discretization is derived with discontinuous (dG) functions in time and a classical continuous Galerkin (cG) method in space.

### 2.1 Notation

We consider a bounded domain  $\Omega \subset \mathbb{R}^2$ . The boundary is partitioned as  $\partial\Omega = \Gamma_N \dot{\cup} \Gamma_D$  where both the Dirichlet boundary  $\Gamma_D$  and the Neumann boundary  $\Gamma_N$  have nonzero Hausdorff measure. Next we define two function spaces,  $V := H_D^1(\Omega; \mathbb{R}^2) \times H^1(\Omega)$  for the displacement field  $u$  and the phase-field  $\varphi$ , and  $Q := L^2(\Gamma_N)$  for the control  $q$ , where

$$\begin{aligned} H^1(\Omega; \mathbb{R}^2) &:= \{v \in L^2(\Omega; \mathbb{R}^2) : D^\alpha v \in L^2(\Omega; \mathbb{R}^2) \ \forall \alpha \in \mathbb{N}_0^2, \ |\alpha| \leq 1\}, \\ H_D^1(\Omega; \mathbb{R}^2) &:= \{v \in H^1(\Omega; \mathbb{R}^2) : v|_{\Gamma_D} = 0\}. \end{aligned}$$

Moreover we consider a bounded time interval  $I = [0, T]$  and introduce the spaces

$$X := \{\mathbf{u} = (u, \varphi) : \mathbf{u} \in L^2(I, V), \ \partial_t \varphi \in L^2(I, H^1(\Omega)^*)\}, \quad W := C(I, Q).$$

Here,  $H^1(\Omega)^*$  denotes the dual space to  $H^1(\Omega)$ , which can be identified via the well-known Hilbert space isomorphism with  $H^1(\Omega)$  such that  $H^1(\Omega)^* \simeq H^1(\Omega)$ .

On  $V$  respectively  $X$  we define the scalar products

$$\begin{aligned} (\mathbf{u}, \mathbf{v}) &:= \int_{\Omega} \mathbf{u} \cdot \mathbf{v} \, dx \quad \forall \mathbf{u}, \mathbf{v} \in V, \\ (\mathbf{u}, \mathbf{v})_I &:= \int_I \int_{\Omega} \mathbf{u} \cdot \mathbf{v} \, dx \, dt = \int_I (\mathbf{u}(t), \mathbf{v}(t)) \, dt \quad \forall \mathbf{u}, \mathbf{v} \in X, \end{aligned}$$

with induced norms  $\|\cdot\|$  and  $\|\cdot\|_I$ , and furthermore the restricted inner products

$$\begin{aligned} (\mathbf{u}(t), \mathbf{v}(t))_{\{\partial_t \varphi(t) > 0\}} &:= \begin{cases} (\mathbf{u}(t), \mathbf{v}(t)), & \partial_t \varphi(t) > 0, \\ 0, & \text{else,} \end{cases} \\ (\mathbf{u}, \mathbf{v})_{\{\partial_t \varphi > 0, I\}} &:= \int_I (\mathbf{u}(t), \mathbf{v}(t))_{\{\partial_t \varphi(t) > 0\}} \, dt \quad \forall \mathbf{u}, \mathbf{v} \in X. \end{aligned}$$

Later we also work with  $(\cdot, \cdot)_{\{\varphi(t_i) > \varphi(t_j)\}}$ , defined like  $(\cdot, \cdot)_{\{\partial_t \varphi(t) > 0\}}$ , and with a semi-linear form  $a(\cdot)(\cdot)$  in which the first argument is nonlinear and the second argument is linear.

## 2.2 Weak formulation

We deal with the following weak formulation: Given  $\mathbf{u}_0 \in V$  and  $q \in W$ , find  $\mathbf{u} \in X$  such that

$$\begin{aligned} (g(\varphi)\mathbb{C}e(\mathbf{u}), e(\Phi_u))_I - (q, \Phi_{u;\perp})_{\Gamma_N, I} &= 0, \\ G_c \varepsilon (\nabla \varphi, \nabla \Phi_\varphi)_I - \frac{G_c}{\varepsilon} (1 - \varphi, \Phi_\varphi)_I + (1 - \kappa)(\varphi \mathbb{C}e(\mathbf{u}) : e(\mathbf{u}), \Phi_\varphi)_I & \\ + \gamma (\partial_t \varphi, \Phi_\varphi)_{\{\partial_t \varphi > 0, I\}} + \eta (\partial_t \varphi, \Phi_\varphi)_I &= 0, \end{aligned} \tag{1}$$

for every test function  $\Phi = (\Phi_u, \Phi_\varphi) \in X$ . Herein  $\Phi_{u;\perp}$  denotes the component of  $\Phi_u$  that is orthogonal to  $\Gamma_N$ . The critical energy release rate is denoted by  $G_c > 0$ . The so-called degradation function  $g(\varphi) := (1 - \kappa)\varphi^2 + \kappa$  helps to extend the displacements to the entire domain  $\Omega$ . The bulk regularization parameter is  $\kappa > 0$ , the phase-field regularization parameter is  $\varepsilon > 0$ , the penalization parameter is  $\gamma > 0$ , and the viscosity parameter is  $0 < \eta \ll \gamma$ . Furthermore,  $\mathbb{C}$  denotes the elasticity tensor and  $e(\mathbf{u})$  the symmetric gradient. Then, we have

$$\mathbb{C}e(\mathbf{u}) = \sigma(\mathbf{u}) = 2\mu e(\mathbf{u}) + \lambda \operatorname{tr}(e(\mathbf{u}))I,$$

where  $\mu, \lambda > 0$  are the Lamé parameters and  $I$  is the identity matrix.

**Remark 2.1.** *The above weak formulation differs slightly from many other phase-field fracture formulations found in the literature since the crack irreversibility constraint  $\partial_t \varphi \leq 0$  is kept on the time-continuous level in order to apply a Galerkin discretization in time.*

**Remark 2.2** (Initial condition  $u_0$ ). *Note that we are concerned with quasi-static brittle fracture without explicit time derivative in the displacement equation. Nonetheless, we introduce for formal reasons  $u_0$ . First, we can develop in an analogous fashion time discretization schemes for the overall forward model. Second, it facilitates the extension to problems in which the displacement equation does have a time derivative, such as dynamic fracture [16, 10]. Third, having  $u_0$  allows for a monolithic implementation structure, and the system matrix for the initial condition is regular.*

**Remark 2.3** (Convexification). *We notice that strict positivity  $\eta > 0$  improves the numerical solution process of (1). In fact, one can show for the quasi-static case that for sufficiently large values of  $\eta$  the control-to-state mapping is single valued due to strict convexity of the energy corresponding to the equation. However, the convexification term  $\eta(\partial_t\varphi, \Phi_\varphi)_I$  also penalizes crack growth. To ensure the dominance of the physically motivated term  $\gamma(\partial_t\varphi, \Phi_\varphi)_{\{\partial_t\varphi>0, I\}}$  we have to choose  $\gamma \gg \eta$ .*

## 2.3 Space-time finite element discretization

### 2.3.1 Temporal discretization

Given  $T > 0$ , we define the time grid  $0 = t_0 < \dots < t_M = T$  to partition the interval  $I$  into  $M$  left-open subintervals  $I_m = (t_{m-1}, t_m]$ ,

$$I = \{0\} \cup I_1 \cup \dots \cup I_M.$$

By using the discontinuous Galerkin method, here dG(0), we seek a solution  $\mathbf{u}$  in the space  $X_k^0$  of piecewise polynomials of degree 0,

$$X_k^0 := \{\mathbf{v} \in X : \mathbf{v}(0) \in V \text{ and } \mathbf{v}|_{I_m} \in \mathbb{P}_0(I_m, V), m = 1, \dots, M\}. \quad (2)$$

Here, the subindex  $k$  indicates the time-discretized function space in order to distinguish it from the continuous space  $X$ . For the jump terms arising in  $X_k^0$  we use the standard notation

$$\mathbf{v}_m^+ := \mathbf{v}(t_m+), \quad \mathbf{v}_m^- := \mathbf{v}(t_m-) = \mathbf{v}(t_m), \quad [\mathbf{v}]_m := \mathbf{v}_m^+ - \mathbf{v}_m^-.$$

**Remark 2.4.** *Since we work with  $dG(0)$ , i.e., piece-wise constant functions in time, we have*

$$\partial_t \mathbf{v} = \mathbf{v}_m^- - \mathbf{v}_{m-1}^+ = 0 \quad \forall \mathbf{v} \in X_k^0 \quad \forall m = 1, \dots, M.$$

The discretized state equation combines the two equations of (1). For a concise formulation, the energy-related terms are expressed as a semi-linear form  $a: Q \times V \times V \rightarrow \mathbb{R}$ ,

$$\begin{aligned} a(q, \mathbf{u})(\Phi) &:= g(\varphi) \cdot (\mathbb{C}e(u), e(\Phi_u)) \\ &+ G_c \varepsilon (\nabla \varphi, \nabla \Phi_\varphi) - \frac{G_c}{\varepsilon} (1 - \varphi, \Phi_\varphi) \\ &+ (1 - \kappa) (\varphi \cdot \mathbb{C}e(u) : e(u), \Phi_\varphi) - (q, \Phi_{u:\perp})_{\Gamma_N}. \end{aligned}$$

Now the fully discretized state equation determines a function  $\mathbf{u} \in X_k^0$  for a given initial value  $\mathbf{u}_0 = (u_0, \varphi_0) \in V$  and a given control  $q \in W$  such that for every  $\Phi \in X_k^0$

$$0 = \sum_{m=1}^M [\gamma(\partial_t\varphi, \Phi_\varphi)_{\{\partial_t\varphi>0, I_m\}} + \eta(\partial_t\varphi, \Phi_\varphi)_{I_m}] \quad (3a)$$

$$+ \sum_{m=0}^{M-1} [\gamma([\varphi]_m, \Phi_{\varphi,m}^+)_{\{\varphi_{m+1}^- > \varphi_m^-\}} + \eta([\varphi]_m, \Phi_{\varphi,m}^+)] \quad (3b)$$

$$+ \sum_{m=1}^M a(q(t_m), \mathbf{u}(t_m))(\Phi(t_m)) \Delta t_m \quad (3c)$$

$$+ (u_0^- - u_0, \Phi_{u,0}^-) + (\varphi_0^- - \varphi_0, \Phi_{\varphi,0}^-). \quad (3d)$$

The time integral in (3c) has been approximated by the right-sided box rule, where  $\Delta t_m := t_m - t_{m-1}$ . Discontinuities of the functions in  $X_k^0$  are captured by the jump terms in (3b) in the typical dG(0) manner. These jump terms can be rewritten as

$$\sum_{m=1}^M [\gamma(\varphi_{m-1}^+ - \varphi_{m-1}^-, \Phi_{\varphi, m-1}^+)_{\{\varphi_m^- > \varphi_{m-1}^-\}} + \eta(\varphi_{m-1}^+ - \varphi_{m-1}^-, \Phi_{\varphi, m-1}^+)]. \quad (4)$$

Moreover, since we are employing a dG(0) scheme, our test functions satisfy

$$\Phi_{m-1}^+ = \Phi_m^- \quad \forall m = 1, \dots, M.$$

Thus the first sum (3a) vanishes entirely by Remark 2.4, and the two terms containing  $\varphi_{m-1}^+$  in (4) become  $(\varphi_m^-, \Phi_{\varphi, m}^-)_{\{\varphi_m^- > \varphi_{m-1}^-\}}$  and  $(\varphi_m^-, \Phi_{\varphi, m}^-)$ , respectively. Together with (3b) and (3d), the discrete state equation (3) is finally written as

$$\begin{aligned} 0 = & \sum_{m=1}^M \left( \gamma[(\varphi_m^-, \Phi_{\varphi, m}^-)_{\{\varphi_m^- > \varphi_{m-1}^-\}} - (\varphi_{m-1}^-, \Phi_{\varphi, m}^-)_{\{\varphi_m^- > \varphi_{m-1}^-\}}] \right. \\ & + \eta[(\varphi_m^-, \Phi_{\varphi, m}^-) - (\varphi_{m-1}^-, \Phi_{\varphi, m}^-)] \\ & \left. + a(q(t_m), \mathbf{u}(t_m))(\Phi(t_m))\Delta t_m \right) \\ & + (u_0^- - u_0, \Phi_{u, 0}^-) + (\varphi_0^- - \varphi_0, \Phi_{\varphi, 0}^-) \quad \forall \Phi \in X_k^0. \end{aligned} \quad (5)$$

To solve (5), we first obtain  $\mathbf{u}_0^- = \mathbf{u}(0)$  from the initial condition

$$(\mathbf{u}(0), \Phi_0^-) = (\mathbf{u}_0, \Phi_0^-) \quad \forall \Phi_0^- \in V. \quad (6)$$

Then we compute  $\mathbf{u}(t_m)$  for  $m = 1, \dots, M$  from

$$\begin{aligned} 0 = & \gamma(\varphi(t_m), \Phi_{\varphi}(t_m))_{\{\varphi(t_m) > \varphi(t_{m-1})\}} + \eta(\varphi(t_m), \Phi_{\varphi}(t_m)) \\ & - \gamma(\varphi(t_{m-1}), \Phi_{\varphi}(t_m))_{\{\varphi(t_m) > \varphi(t_{m-1})\}} - \eta(\varphi(t_{m-1}), \Phi_{\varphi}(t_m)) \\ & + a(q(t_m), \mathbf{u}(t_m))(\Phi(t_m))\Delta t_m \quad \forall \Phi \in X_k^0. \end{aligned} \quad (7)$$

### 2.3.2 Spatial discretization

For the spatial discretization, we employ again a Galerkin finite element scheme by introducing  $H^1$  conforming discrete spaces. We consider two-dimensional shape-regular meshes with quadrilateral elements  $K$  forming the mesh  $\mathcal{T}_h = \{K\}$ ; see [20]. The spatial discretization parameter is the diameter  $h_K$  of the element  $K$ . On the mesh  $\mathcal{T}_h$  we construct a finite element space  $V_h := V_{uh} \times V_{\varphi h}$  as usual:

$$\begin{aligned} V_{uh} &:= \{v \in H_D^1(\Omega; \mathbb{R}^2) : v|_K \in Q_s(K) \text{ for } K \in \mathcal{T}_h\}, \\ V_{\varphi h} &:= \{v \in H^1(\Omega) : v|_K \in Q_s(K) \text{ for } K \in \mathcal{T}_h\}. \end{aligned}$$

Herein  $Q_s(K)$  consists of shape functions that are obtained as bilinear transformations of functions defined on the master element  $\hat{K} = (0, 1)^2$ , where  $\hat{Q}_s(\hat{K})$  is the space of tensor product polynomials up to degree  $s$  in dimension  $d$ , defined as

$$\hat{Q}_s(\hat{K}) := \text{span} \left\{ \prod_{i=1}^d \hat{x}_i^{\alpha_i} : \alpha_i \in \{0, 1, \dots, s\} \right\}.$$

Specifically, for  $s = 1$  and  $d = 2$  we have

$$\hat{Q}_1(\hat{K}) = \text{span}\{1, \hat{x}_1, \hat{x}_2, \hat{x}_1\hat{x}_2\}.$$

With these preparations, based on (2), we now design the fully discrete function space

$$X_{hk}^0 := \{\mathbf{v} \in X : \mathbf{v}_h(0) \in V_h \text{ and } \mathbf{v}|_{I_m} \in \mathbb{P}_0(I_m, V_h), m = 1, \dots, M\}.$$

The discrete control space  $Q_h$  is constructed like  $X_{hk}^0$  using  $Q_1(K)$  (again  $s = 1$ ) elements, but restricted to the Neumann boundary  $\Gamma_N$ . Then, the fully discrete system consists of the initial condition

$$(\mathbf{u}_h(0), \Phi_{h,0}^-) = (\mathbf{u}_{h,0}, \Phi_{h,0}^-) \quad \forall \Phi_{h,0}^- \in V_h \quad (8)$$

and for  $m = 1, \dots, M$  of the local system

$$\begin{aligned} 0 = & \gamma(\varphi_h(t_m), \Phi_{\varphi,h}(t_m))_{\{\varphi_h(t_m) > \varphi_h(t_{m-1})\}} + \eta(\varphi_h(t_m), \Phi_{\varphi,h}(t_m)) \\ & - \gamma(\varphi_h(t_{m-1}), \Phi_{\varphi,h}(t_m))_{\{\varphi_h(t_m) > \varphi_h(t_{m-1})\}} - \eta(\varphi_h(t_{m-1}), \Phi_{\varphi,h}(t_m)) \\ & + a(q_h(t_m), \mathbf{u}_h(t_m))(\Phi_h(t_m))\Delta t_m \quad \forall \Phi_h \in X_{hk}^0. \end{aligned} \quad (9)$$

### 3 Optimization with phase-field fracture

In this section, we state the phase-field optimal control problem and introduce the reduced solution approach. Therein, the primal forward problem plus three additional equations must be solved. Their combination yields the final solution algorithm.

#### 3.1 Optimization problem

We consider a separable NLP (Non-Linear Program) with a cost functional of tracking type. In this tracking type functional, the objective is to approximate a given phase-field fracture pattern  $\varphi_d$  by determining a suitable control  $q$ . The corresponding minimization problem is given by:

$$\begin{aligned} \min_{q, \mathbf{u}} \quad \mathcal{J}(q, \mathbf{u}) &:= \frac{1}{2} \sum_{m=1}^M \|\varphi(t_m) - \varphi_d(t_m)\|^2 + \frac{\alpha}{2} \sum_{m=1}^M \|q(t_m) - q_d(t_m)\|_{\Gamma_N}^2 \\ \text{s.t.} \quad & (6) \text{ and } (7) \text{ for } m = 1, \dots, M, \text{ with } (u_0, \varphi_0) \in V \text{ and } (q, \mathbf{u}) \in W \times X, \end{aligned} \quad (10)$$

where  $\varphi_d \in L^\infty(\Omega)$  is some desired phase-field and  $q_d$  is a suitable nominal control that we use for numerical stabilization. The second sum represents a common Tikhonov regularization with parameter  $\alpha$ . The existence of a global solution of (10) in  $L^2(I, Q) \times X$  has been shown in [51, Theorem 4.3] for functions that are non-negative and weakly semi-continuous.

**Remark 3.1.** *The fully discrete version of (10) is obtained by working with the equations (8) and (9). In what follows, in order to keep the notation comfortable, we omit the index  $h$  indicating the spatial discretization.*



### 3.2 Reduced optimization problem

In order to handle (10) by the reduced approach, we assume that a solution operator  $S: W \rightarrow X$  exists for the PDE (1). The cost functional  $\mathcal{J}(q, \mathbf{u})$  then reduces to  $j: W \rightarrow \mathbb{R}$ ,  $j(q) := \mathcal{J}(q, S(q))$ , and we replace (10) by the unconstrained optimization problem

$$\min_q j(q). \quad (11)$$

To solve  $j'(q) = 0$  by Newton's method, we compute representations of  $j'$  and  $j''$  using the established approach in [8]. It requires the solution of four equations (given below) for derivatives of the Lagrangian  $\mathcal{L}: W \times X_k^0 \times X_k^0 \rightarrow \mathbb{R}$ , which is defined within the dG( $r$ ) setting as

$$\begin{aligned} \mathcal{L}(q, \mathbf{u}, \mathbf{z}) := & \mathcal{J}(q, \mathbf{u}) - \sum_{m=1}^M \left( \gamma(\partial_t \varphi, z_\varphi)_{\{\partial_t \varphi > 0, I_m\}} + \eta(\partial_t \varphi, z_\varphi)_{I_m} \right) \\ & - \sum_{m=0}^{M-1} \left( \gamma([\varphi]_m, z_{\varphi, m}^+)_{\{\varphi_{m+1}^- > \varphi_m^-\}} + \eta([\varphi]_m, z_{\varphi, m}^+) \right) \\ & - \int_I a(q(t), \mathbf{u}(t))(\mathbf{z}(t)) dt \\ & - \eta_0(u(0) - u_0, z_u(0)) - \eta(\varphi(0) - \varphi_0, z_\varphi(0)), \end{aligned} \quad (12)$$

and for the time continuous case as

$$\begin{aligned} \mathcal{L}(q, \mathbf{u}, \mathbf{z}) := & \mathcal{J}(q, \mathbf{u}) - \gamma(\partial_t \varphi, z_\varphi)_{\{\partial_t \varphi > 0, I\}} - \eta(\partial_t \varphi, z_\varphi)_I \\ & - \int_I a(q(t), \mathbf{u}(t))(\mathbf{z}(t)) dt \\ & - \eta_0(u(0) - u_0, z_u(0)) - \eta(\varphi(0) - \varphi_0, z_\varphi(0)). \end{aligned} \quad (13)$$

**Remark 3.2.** We notice that starting with (12) and deriving the state, adjoint, tangent, adjoint Hessian equations, exhibits the property that discretization and optimization interchange, i.e., the discretize-then-optimize and the optimize-then-discretize approaches are equal; see [8, 42] for parabolic optimization problems. However in what follows, we start from the time-continuous formulation (13) for the ease of presentation (which nonetheless becomes difficult enough) and we add only afterwards the dG-in-time representations, which yields in the end the same result if we had started with (12).

### 3.3 State, adjoint, tangent, adjoint Hessian

In this section we state the four equations to be solved for computing  $j'$  and  $j''$ .

1. *State equation:* given  $q \in W$ , find  $\mathbf{u} = S(q) \in X$  such that the PDE (1) holds:

$$\mathcal{L}'_{\mathbf{z}}(q, \mathbf{u}, \mathbf{z})(\Phi) = 0 \quad \forall \Phi \in X.$$

2. *Adjoint equation:* given  $q \in W$  and  $\mathbf{u} = S(q)$ , find  $\mathbf{z} \in X$  such that

$$\mathcal{L}'_{\mathbf{u}}(q, \mathbf{u}, \mathbf{z})(\Phi) = 0 \quad \forall \Phi \in X. \quad (14)$$

3. *Tangent equation:* given  $q \in W$ ,  $\mathbf{u} = S(q)$ , and a direction  $\delta q \in W$ , find  $\delta \mathbf{u} \in X$  such that

$$\mathcal{L}_{qz}''(q, \mathbf{u}, z)(\delta q, \Phi) + \mathcal{L}_{uz}''(q, \mathbf{u}, z)(\delta \mathbf{u}, \Phi) = 0 \quad \forall \Phi \in X. \quad (15)$$

4. *Adjoint Hessian equation:* given  $q \in W$ ,  $\mathbf{u} = S(q)$ ,  $z \in X$  from (14), a direction  $\delta q \in W$ , and  $\delta \mathbf{u} \in X$  from (15), find  $\delta z \in X$  such that

$$\mathcal{L}_{qu}''(q, \mathbf{u}, z)(\delta q, \Phi) + \mathcal{L}_{uu}''(q, \mathbf{u}, z)(\delta \mathbf{u}, \Phi) + \mathcal{L}_{zu}''(q, \mathbf{u}, z)(\delta z, \Phi) = 0 \quad \forall \Phi \in X. \quad (16)$$

Solving these equations in a specific order (see for instance [8, 42]) leads to the following representations of the derivatives that we need for Newton's method:

$$\begin{aligned} j'(q)(\delta q) &= \mathcal{L}'_q(q, \mathbf{u}, z)(\delta q) \quad \forall \delta q \in W, \\ j''(q)(\delta q_1, \delta q_2) &= \mathcal{L}_{qq}''(q, \mathbf{u}, z)(\delta q_1, \delta q_2) + \mathcal{L}_{uq}''(q, \mathbf{u}, z)(\delta \mathbf{u}, \delta q_2) \\ &\quad + \mathcal{L}_{zq}''(q, \mathbf{u}, z)(\delta z, \delta q_2) \quad \forall \delta q_1, \delta q_2 \in W. \end{aligned} \quad (17)$$

## 4 Auxiliary equations

Starting from the Lagrangian (13), we derive in detail the three auxiliary equations (14)–(16). Specific emphasis is on the regularization terms for the crack irreversibility and the convexification.

### 4.1 Adjoint

In the adjoint for  $dG(0)$  we seek  $z = (z_u, z_\varphi) \in X_k^0$  such that

$$\mathcal{L}'_u(q, \mathbf{u}, z)(\Phi) = 0 \quad \forall \Phi \in X_k^0.$$

The first interesting part is the calculation of the derivative of  $\mathcal{L}$ . We formulate it directly in the weak form

$$\begin{aligned} \mathcal{L}'_u(q, \mathbf{u}, z)(\Phi) &= \mathcal{J}'_u(q, \mathbf{u})(\Phi) \\ &\quad - \gamma(\partial_t \Phi_\varphi, z_\varphi)_{\{\partial_t \varphi > 0, I\}} - \eta(\partial_t \Phi_\varphi, z_\varphi)_I \\ &\quad - \int_I a'_u(q(t), \mathbf{u}(t))(\Phi(t), z(t)) dt \\ &\quad - \eta_0(\Phi_u(0), z_u(0)) - \eta(\Phi_\varphi(0), z_\varphi(0)). \end{aligned} \quad (18)$$

**Remark 4.1.** We notice that  $\gamma(\partial_t \Phi_\varphi, z_\varphi)_{\{\partial_t \varphi > 0, I\}}$  is a suitable numerical approximation to the derivative of  $\gamma(\partial_t \varphi, z_\varphi)_{\{\partial_t \varphi > 0, I\}}$ , since formally a characteristic function must be differentiated; see also [49, Section 5] for a similar numerical approximation in the context of a related forward problem. The same procedure as numerical approximation of the derivative is utilized in the other three auxiliary problems, namely the adjoint, tangent, and adjoint Hessian.

The partial derivative of  $a$  in (18) reads

$$\begin{aligned} a'_u(q, \mathbf{u})(\Phi, z) &= ((1 - \kappa)\varphi^2 + \kappa) \cdot (\mathbb{C}e(\Phi_u), e(z_u)) \\ &\quad + 2\varphi(1 - \kappa)\Phi_\varphi(\mathbb{C}e(u), e(z_u)) \\ &\quad + G_c \varepsilon (\nabla \Phi_\varphi, \nabla z_\varphi) + \frac{G_c}{\varepsilon}(\Phi_\varphi, z_\varphi) \\ &\quad + (1 - \kappa)(\Phi_\varphi \cdot \mathbb{C}e(u) : e(u), z_\varphi) \\ &\quad + 2\varphi(1 - \kappa)(\mathbb{C}e(\Phi_u) : e(u), z_\varphi). \end{aligned} \quad (19)$$

Now the main problem is that the time derivatives are applied to the test function  $\Phi$  as usual in the adjoint. Therefore we use integration by parts to shift the time derivatives over to  $\mathbf{z}$ . Then the second line in (18) becomes

$$\begin{aligned} & \gamma(\Phi_\varphi, \partial_t z_\varphi)_{\{\partial_t \varphi > 0, I\}} + \eta(\Phi_\varphi, \partial_t z_\varphi)_I \\ & + \gamma(\Phi_\varphi(0), z_\varphi(0))_{\{\partial_t \varphi(0) > 0\}} + \eta(\Phi_\varphi(0), z_\varphi(0)) \\ & - \gamma(\Phi_\varphi(T), z_\varphi(T))_{\{\partial_t \varphi(T) > 0\}} - \eta(\Phi_\varphi(T), z_\varphi(T)). \end{aligned} \quad (20)$$

At this point we have to decide how to approximate the time derivative  $\partial_t \varphi(0)$ . While  $\partial_t \varphi(t_m)$  for  $m = 1, \dots, M$  is easily approximated by the backward difference

$$\partial_t \varphi(t_m) \approx \frac{\varphi(t_m) - \varphi(t_{m-1})}{t_m - t_{m-1}},$$

this procedure will not work for the first mesh point  $t_0 = 0$ . The forward difference

$$\partial_t \varphi(0) \approx \frac{\varphi(t_1) - \varphi(t_0)}{t_1 - t_0}$$

is a good choice because it simplifies the condition  $\partial_t \varphi(t_0) > 0$  to  $\varphi(t_1) > \varphi(t_0)$  and leads to desired cancelations in (21). Now we will repeat the procedure that we applied to the state equation. We approximate the time derivatives and add the jump terms (with shifted index) as we did in (3), obtaining expressions similar to (4):

$$\begin{aligned} \mathcal{L}'_{\mathbf{u}}(q, \mathbf{u}, \mathbf{z})(\Phi) &= \mathcal{J}'_{\mathbf{u}}(q, \mathbf{u})(\Phi) \\ &+ \sum_{m=1}^M [\gamma(\Phi_{\varphi, m}^-, z_{\varphi, m}^- - z_{\varphi, m-1}^+)_{\{\varphi_m^- > \varphi_{m-1}^-\}} \\ &\quad + \eta(\Phi_{\varphi, m}^-, z_{\varphi, m}^- - z_{\varphi, m-1}^+)] \\ &- \gamma(\Phi_{\varphi, M}^-, z_{\varphi, M}^-)_{\{\varphi(t_M) > \varphi(t_{M-1})\}} - \eta(\Phi_{\varphi, M}^-, z_{\varphi, M}^-) \\ &+ \gamma(\Phi_{\varphi, 0}^-, z_{\varphi, 0}^-)_{\{\varphi(t_1) > \varphi(t_0)\}} + \eta(\Phi_{\varphi, 0}^-, z_{\varphi, 0}^-) \\ &+ \sum_{m=1}^M [\gamma(\Phi_{\varphi, m-1}^-, z_{\varphi, m-1}^+ - z_{\varphi, m-1}^-)_{\{\varphi_m^- > \varphi_{m-1}^-\}} \\ &\quad + \eta(\Phi_{\varphi, m-1}^-, z_{\varphi, m-1}^+ - z_{\varphi, m-1}^-)] \\ &- \sum_{m=1}^M a'_{\mathbf{u}}(q(t_m), \mathbf{u}(t_m))(\Phi(t_m), \mathbf{z}(t_m)) \Delta t_m \\ &- \eta_0(\Phi_{u, 0}^-, z_{u, 0}^-) - \eta(\Phi_{\varphi, 0}^-, z_{\varphi, 0}^-). \end{aligned} \quad (21)$$

Since  $z_\varphi \in X_k^0$ , we have  $z_{\varphi, m}^- = z_{\varphi, m-1}^+$  and see that the first sum vanishes entirely. We also see that the terms  $\pm \eta(\Phi_{\varphi, 0}^-, z_{\varphi, 0}^-)$  in the fifth and the last line of (21) cancel. Moreover, we assume that  $\varphi(t_1) \leq \varphi(t_0)$  in the initial step, and hence the term  $\gamma(\Phi_{\varphi, 0}^-, z_{\varphi, 0}^-)_{\{\varphi(t_1) > \varphi(t_0)\}}$  in the fifth line vanishes as well.

**Remark 4.2** (Projection of the initial solution). *The assumption  $\varphi(t_1) \leq \varphi(t_0)$  is numerically justified since at  $t_0$  some initial phase-field solution is prescribed. From  $t_0$  to  $t_1$  an  $L^2$  projection of the initial conditions is employed that conserves the crack irreversibility constraint.*

By the above arguments we eliminate the second, third and fifth line of (21) and the second term of the last line, whereas the initial values for  $z_u$  are still present:

$$\begin{aligned}
\mathcal{L}'_u(q, \mathbf{u}, \mathbf{z})(\Phi) &= \mathcal{J}'_u(q, \mathbf{u})(\Phi) \\
&\quad - \gamma(\Phi_{\varphi, M}^-, z_{\varphi, M}^-)_{\{\varphi(t_M) > \varphi(t_{M-1})\}} - \eta(\Phi_{\varphi, M}^-, z_{\varphi, M}^-) \\
&\quad + \sum_{m=1}^M [\gamma(\Phi_{\varphi, m-1}^-, z_{\varphi, m-1}^+ - z_{\varphi, m-1}^-)_{\{\varphi_m^- > \varphi_{m-1}^-\}} \\
&\quad \quad + \eta(\Phi_{\varphi, m-1}^-, z_{\varphi, m-1}^+ - z_{\varphi, m-1}^-)] \\
&\quad - \sum_{m=1}^M a'_u(q(t_m), \mathbf{u}(t_m))(\Phi(t_m), \mathbf{z}(t_m)) \Delta t_m \\
&\quad - \eta_0(\Phi_{u, 0}^-, z_{u, 0}^-).
\end{aligned} \tag{22}$$

## 4.2 Adjoint time-stepping scheme

From here on we exploit the separable structure of  $\mathcal{J}(q, \mathbf{u}) = \sum_m J(q(t_m), \mathbf{u}(t_m))$ . We start the solution process by pulling out from (22) every term associated with the last time point  $t_M$ :

$$\begin{aligned}
&a'_u(q(t_M) \mathbf{u}(t_M))(\Phi(t_M), \mathbf{z}(t_M)) \Delta t_M \\
&\quad + \gamma(\Phi_{\varphi, M}^-, z_{\varphi, M}^-)_{\{\varphi_m^- > \varphi_{m-1}^-\}} + \eta(\Phi_{\varphi, M}^-, z_{\varphi, M}^-) \\
&= J'_u(q(t_M), \mathbf{u}(t_M))(\Phi(t_M)) \quad \forall \Phi \in X_k^0.
\end{aligned} \tag{23}$$

Now we collect what is left, multiply by  $-1$  and use the  $X_k^0$  property ( $z_{\varphi, m-1}^+ = z_{\varphi, m}^-$ ):

$$\begin{aligned}
0 &= \sum_{m=1}^M [\gamma(\Phi_{\varphi, m-1}^-, z_{\varphi, m-1}^- - z_{\varphi, m}^-)_{\{\varphi_m^- > \varphi_{m-1}^-\}} + \eta(\Phi_{\varphi, m-1}^-, z_{\varphi, m-1}^- - z_{\varphi, m}^-)] \\
&\quad + \sum_{m=1}^{M-1} a'_u(q(t_m), \mathbf{u}(t_m))(\Phi(t_m), \mathbf{z}(t_m)) \Delta t_m \\
&\quad - \sum_{m=1}^{M-1} J'_u(q(t_m), \mathbf{u}(t_m))(\Phi(t_m)) \\
&\quad + \eta_0(\Phi_{u, 0}^-, z_{u, 0}^-) \quad \forall \Phi \in X_k^0.
\end{aligned} \tag{24}$$

To formulate the equations that are actually solved in every time step we want to rewrite the entire equation as a single sum. Therefore we shift down the index of the first sum (the jump terms), take out the terms for  $m = 0$ , and obtain

$$\begin{aligned}
0 &= \sum_{m=1}^{M-1} \left( [\gamma(\Phi_{\varphi, m}^-, z_{\varphi, m}^- - z_{\varphi, m+1}^-)_{\{\varphi_{m+1}^- > \varphi_m^-\}} + \eta(\Phi_{\varphi, m}^-, z_{\varphi, m}^- - z_{\varphi, m+1}^-)] \right. \\
&\quad \quad + a'_u(q(t_m), \mathbf{u}(t_m))(\Phi(t_m), \mathbf{z}(t_m)) \Delta t_m \\
&\quad \quad \left. - J'_u(q(t_m), \mathbf{u}(t_m))(\Phi(t_m)) \right) \\
&\quad + \gamma(\Phi_{\varphi, 0}^-, z_{\varphi, 0}^- - z_{\varphi, 1}^-)_{\{\varphi_1^- > \varphi_0^-\}} + \eta(\Phi_{\varphi, 0}^-, z_{\varphi, 0}^- - z_{\varphi, 1}^-) \\
&\quad + \eta_0(\Phi_{u, 0}^-, z_{u, 0}^-).
\end{aligned}$$

Now we solve for  $m = M - 1, M - 2, \dots, 1$  the equation

$$\begin{aligned} & a'_u(q(t_m), \mathbf{u}(t_m))(\Phi(t_m), \mathbf{z}(t_m))\Delta t_m \\ & + \gamma(\Phi_{\varphi, m}^-, z_{\varphi, m}^- - z_{\varphi, m+1}^-)_{\{\varphi_{m+1}^- > \varphi_m^-\}} + \eta(\Phi_{\varphi, m}^-, z_{\varphi, m}^- - z_{\varphi, m+1}^-) \\ & = J'_u(q(t_m), \mathbf{u}(t_m))(\Phi(t_m)) \quad \forall \Phi \in X_k^0. \end{aligned} \quad (25)$$

Finally three terms are left for  $m = 0$ ,

$$\gamma(\Phi_{\varphi, 0}^-, z_{\varphi, 0}^- - z_{\varphi, 1}^-)_{\{\varphi_1^- > \varphi_0^-\}} + \eta(\Phi_{\varphi, 0}^-, z_{\varphi, 0}^- - z_{\varphi, 1}^-) + \eta_0(\Phi_{u, 0}^-, z_{u, 0}^-) = 0. \quad (26)$$

For  $\eta_0 \ll \eta$  small enough the last term of (26) can be dropped and the following equation can be solved instead:

$$(\Phi_{\varphi, 0}^-, z_{\varphi, 1}^-) = (\Phi_{\varphi, 0}^-, z_{\varphi, 0}^-). \quad (27)$$

**Remark 4.3** (Algorithmic realization). *To avoid singular matrices that would lead to a loss of convergence in the linear solvers, we have to add an initial condition for  $z_{u, 0}^-$ :  $(\Phi_{u, 0}^-, z_{u, 1}^-) = (\Phi_{u, 0}^-, z_{u, 0}^-)$ . In total we replace (27) by  $(\Phi_0^-, \mathbf{z}_1^-) = (\Phi_0^-, \mathbf{z}_0^-)$ . We also refer the reader to the third reason outlined in Remark 2.2.*

### 4.3 Tangent equation

The second auxiliary equation is the tangent equation. In this equation we seek  $\delta \mathbf{u} = (\delta u, \delta \varphi) \in X_k^0$  such that

$$\mathcal{L}_{qz}''(q, \mathbf{u}, \mathbf{z})(\delta q, \Phi) + \mathcal{L}_{uz}''(q, \mathbf{u}, \mathbf{z})(\delta \mathbf{u}, \Phi) = 0 \quad \forall \Phi \in X_k^0.$$

Here we will apply the same procedure as for the state equation. Recall that  $\mathcal{L}(q, \mathbf{u}, \mathbf{z})$  contains the integrand  $a(q(t), \mathbf{u}(t))(\mathbf{z}(t))$  with  $\mathbf{z}(t)$  entering linearly. Hence the partial derivative required for  $\mathcal{L}_{uz}''(q, \mathbf{u}, \mathbf{z})(\delta \mathbf{u}, \Phi)$  is simply  $a'_u(q, \mathbf{u})(\delta \mathbf{u}, \Phi)$ , and the partial derivative required for  $\mathcal{L}_{qz}''(q, \mathbf{u}, \mathbf{z})(\delta q, \Phi)$  can be derived from (2.3.1) as

$$a'_q(q, \mathbf{u})(\delta q, \Phi) = -(\delta q, \Phi_{u, y})_{\Gamma_N}. \quad (28)$$

Furthermore,  $\mathcal{J}(q, \mathbf{u})$  does not depend on  $\mathbf{z}$ , hence  $\mathcal{J}_{qz}''$  and  $\mathcal{J}_{uz}''$  vanish. Using the right-sided box rule again, we thus obtain the discretized tangent equation

$$\begin{aligned} 0 &= \sum_{m=1}^M [\gamma(\delta \varphi_m^- - \delta \varphi_{m-1}^+, \Phi_{\varphi, m}^-)_{\{\varphi_m^- > \varphi_{m-1}^-\}} + \eta(\delta \varphi_m^- - \delta \varphi_{m-1}^+, \Phi_{\varphi, m}^-)] \\ &+ \sum_{m=1}^M a'_u(q(t_m), \mathbf{u}(t_m))(\delta \mathbf{u}(t_m), \Phi(t_m))\Delta t_m \\ &+ \sum_{m=0}^{M-1} [\gamma(\delta \varphi_m^+ - \delta \varphi_m^-, \Phi_{\varphi, m}^+)_{\{\varphi_{m+1}^- > \varphi_m^-\}} + \eta(\delta \varphi_m^+ - \delta \varphi_m^-, \Phi_{\varphi, m}^+)] \\ &+ \eta_0(\delta u_0^-, \Phi_{u, 0}^-) + \eta(\delta \varphi_0^-, \Phi_{\varphi, 0}^-) \\ &+ \sum_{m=1}^M a'_q(q(t_m), \mathbf{u}(t_m))(\delta q(t_m), \Phi(t_m))\Delta t_m \quad \forall \Phi \in X_k^0. \end{aligned} \quad (29)$$

It is clear that the first sum is zero due to the dG(0) property. By shifting the index of the third sum in (29) and applying the dG(0) property to  $\Phi_{\varphi,m-1}^+$  we can combine the last three sums and rewrite (29) as

$$\begin{aligned}
0 = & \sum_{m=1}^M \left( a'_u(q(t_m), \mathbf{u}(t_m))(\delta \mathbf{u}(t_m), \Phi(t_m)) \Delta t_m \right. \\
& + \gamma(\delta \varphi_{m-1}^+ - \delta \varphi_{m-1}^-, \Phi_{\varphi,m}^-)_{\{\varphi_m^- > \varphi_{m-1}^-\}} \\
& + \eta(\delta \varphi_{m-1}^+ - \delta \varphi_{m-1}^-, \Phi_{\varphi,m}^-) \\
& \left. + a'_q(q(t_m), \mathbf{u}(t_m))(\delta q(t_m), \Phi(t_m)) \Delta t_m \right) \\
& + \eta_0(\delta u_0^-, \Phi_{u,0}^-) + \eta(\delta \varphi_0^-, \Phi_{\varphi,0}^-) \quad \forall \Phi \in X_k^0.
\end{aligned} \tag{30}$$

#### 4.4 Tangent time-stepping schemes

As in the state equation we first solve the initial conditions,

$$\begin{aligned}
(\delta u_0^-, \Phi_{u,0}^-) &= 0, \\
(\delta \varphi_0^-, \Phi_{\varphi,0}^-) &= 0,
\end{aligned}$$

in short

$$(\delta \mathbf{u}(t_0), \Phi_0^-) = 0 \quad \forall \Phi_0^- \in V. \tag{31}$$

Applying the  $X_k^0$  property to  $\delta \varphi_{m-1}^+$  we can finally solve for  $m = 1, \dots, M$  the following equation

$$\begin{aligned}
& \gamma(\delta \varphi_m^-, \Phi_{\varphi,m}^-)_{\{\varphi_m^- > \varphi_{m-1}^-\}} + \eta(\delta \varphi_m^-, \Phi_{\varphi,m}^-) \\
& + a'_u(q(t_m), \mathbf{u}(t_m))(\delta \mathbf{u}(t_m), \Phi(t_m)) \Delta t_m \\
& = \eta(\delta \varphi_{m-1}^-, \Phi_{\varphi,m}^-) + \gamma(\delta \varphi_{m-1}^-, \Phi_{\varphi,m}^-)_{\{\varphi_m^- > \varphi_{m-1}^-\}} \\
& - a'_q(q(t_m), \mathbf{u}(t_m))(\delta q(t_m), \Phi(t_m)) \Delta t_m \quad \forall \Phi \in X_k^0.
\end{aligned} \tag{32}$$

#### 4.5 Adjoint Hessian equation

The third and last auxiliary equation is the adjoint Hessian equation. In this equation we seek  $\delta \mathbf{z} = (\delta z_u, \delta z_\varphi) \in X_k^0$  such that for all  $\Phi \in X_k^0$  the following equation holds true:

$$\mathcal{L}_{qu}''(q, \mathbf{u}, \mathbf{z})(\delta q, \Phi) + \mathcal{L}_{uu}''(q, \mathbf{u}, \mathbf{z})(\delta \mathbf{u}, \Phi) + \mathcal{L}_{zu}''(q, \mathbf{u}, \mathbf{z})(\delta \mathbf{z}, \Phi) = 0. \tag{33}$$

First we see that  $\mathcal{L}_{qu}''(q, \mathbf{u}, \mathbf{z})(\delta q, \Phi) = 0$  since  $q$  and  $\mathbf{u}$  are decoupled. The derivative of  $a$  in  $\mathcal{L}_{zu}''(q, \mathbf{u}, \mathbf{z})(\delta \mathbf{z}, \Phi)$  is given by  $a'_u(q, \mathbf{u})(\Phi, \delta \mathbf{z})$  due to the linearity of  $\mathbf{z}$  in  $a$ . However, a genuine second-order derivative of  $a$  arises in  $\mathcal{L}_{uu}''(q, \mathbf{u}, \mathbf{z})(\delta \mathbf{u}, \Phi)$ :

$$\begin{aligned}
a''_{uu}(q, \mathbf{u})(\delta \mathbf{u}, \Phi, \mathbf{z}) &= 2\varphi \cdot (1 - \kappa) \Phi_\varphi \cdot (\mathbb{C}e(\delta u), e(z_u)) \\
& + 2\delta \varphi \cdot (1 - \kappa) (\mathbb{C}e(u), e(z_u)) \cdot \Phi_\varphi \\
& + 2\varphi \cdot (1 - \kappa) (\mathbb{C}e(u), e(z_u)) \delta \varphi \\
& + 2\varphi \cdot (1 - \kappa) (\mathbb{C}e(\Phi_u) : e(\delta u), z_\varphi) \\
& + 2\delta \varphi \cdot (1 - \kappa) (\mathbb{C}e(\Phi_u) : e(u), z_\varphi) \\
& + 2(\mathbb{C}e(\delta u) : e(u), z_\varphi) \cdot \Phi_\varphi.
\end{aligned} \tag{34}$$

Now we can rewrite (33) in a dG(0) setting:

$$\begin{aligned}
0 = & \sum_{m=1}^M J''_{\mathbf{u}\mathbf{u}}(q(t_m), \mathbf{u}(t_m))(\delta \mathbf{u}(t_m), \Phi(t_m)) \\
& - \sum_{m=1}^M a''_{\mathbf{u}\mathbf{u}}(q(t_m), \mathbf{u}(t_m))(\delta \mathbf{u}(t_m), \Phi(t_m), \mathbf{z}(t_m))\Delta t_m \\
& + \sum_{m=1}^M [\gamma(\Phi_{\varphi,m}^-, \delta z_{\varphi,m}^- - \delta z_{\varphi,m-1}^+)_{\{\varphi_m^- > \varphi_{m-1}^-\}} + \eta(\Phi_{\varphi,m}^-, z_{\varphi,m}^- - z_{\varphi,m-1}^+)] \\
& - \gamma(\Phi_{\varphi,M}^-, \delta z_{\varphi,M}^-)_{\{\varphi_M^- > \varphi_{M-1}^-\}} - \eta(\Phi_{\varphi,M}^-, \delta z_{\varphi,M}^-) \\
& + \gamma(\Phi_{\varphi,0}^-, \delta z_{\varphi,0}^-)_{\{\varphi_1^- > \varphi_0^-\}} + \eta(\Phi_{\varphi,0}^-, \delta z_{\varphi,0}^-) \\
& - \sum_{m=1}^M a'_{\mathbf{u}}(q(t_m), \mathbf{u}(t_m))(\Phi(t_m), \delta \mathbf{z}(t_m))\Delta t_m \\
& + \sum_{m=0}^{M-1} \gamma(\Phi_{\varphi,m}^-, \delta z_{\varphi,m}^+ - \delta z_{\varphi,m}^-)_{\{\varphi_{m+1}^- > \varphi_m^-\}} + \eta(\Phi_{\varphi,m}^-, \delta z_{\varphi,m}^+ - \delta z_{\varphi,m}^-) \\
& - \eta_0(\Phi_{u,0}^-, \delta z_{u,0}^-) - \eta(\Phi_{\varphi,0}^-, \delta z_{\varphi,0}^-) \quad \forall \Phi \in X_k^0.
\end{aligned} \tag{35}$$

Note that the same scaling of initial data was applied that we already used for the adjoint equation. By the  $X_k^0$  property the third sum vanishes entirely. Due to Remark 4.2 and the cancelation of  $\pm \eta(\Phi_{\varphi,0}^-, \delta z_{\varphi,0}^-)$  the fifth line vanishes as well. By shifting the index of the jump terms we can rewrite the equation as:

$$\begin{aligned}
0 = & \sum_{m=1}^M \left( J''_{\mathbf{u}\mathbf{u}}(q(t_m), \mathbf{u}(t_m))(\delta \mathbf{u}(t_m), \Phi(t_m)) \right. \\
& - a''_{\mathbf{u}\mathbf{u}}(q(t_m), \mathbf{u}(t_m))(\delta \mathbf{u}(t_m), \Phi(t_m), \mathbf{z}(t_m))\Delta t_m \\
& - a'_{\mathbf{u}}(q(t_m), \mathbf{u}(t_m))(\Phi(t_m), \delta \mathbf{z}(t_m))\Delta t_m \\
& + \gamma(\Phi_{\varphi,m-1}^-, \delta z_{\varphi,m-1}^+ - \delta z_{\varphi,m-1}^-)_{\{\varphi_m^- > \varphi_{m-1}^-\}} \\
& \left. + \eta(\Phi_{\varphi,m-1}^-, \delta z_{\varphi,m-1}^+ - \delta z_{\varphi,m-1}^-) \right) \\
& - \gamma(\Phi_{\varphi,M}^-, \delta z_{\varphi,M}^-)_{\{\varphi_M^- > \varphi_{M-1}^-\}} - \eta(\Phi_{\varphi,M}^-, \delta z_{\varphi,M}^-) \\
& - \eta_0(\Phi_{u,0}^-, \delta z_{u,0}^-) \quad \forall \Phi \in X_k^0.
\end{aligned} \tag{36}$$

#### 4.6 Adjoint Hessian time-stepping schemes

As in the adjoint time-stepping scheme we first collect all terms that contain the last time point  $t_M$  and solve

$$\begin{aligned}
0 = & J''_{\mathbf{u}\mathbf{u}}(q(t_M), \mathbf{u}(t_M))(\delta \mathbf{u}(t_M), \Phi(t_M)) \\
& - a'_{\mathbf{u}}(q(t_M), \mathbf{u}(t_M))(\Phi(t_M), \delta \mathbf{z}(t_M))\Delta t_M \\
& - a''_{\mathbf{u}\mathbf{u}}(q(t_M), \mathbf{u}(t_M))(\delta \mathbf{u}(t_M), \Phi(t_M), \mathbf{z}(t_M))\Delta t_M \\
& - \gamma(\Phi_{\varphi,M}^-, \delta z_{\varphi,M}^-)_{\{\varphi_M^- > \varphi_{M-1}^-\}} - \eta(\Phi_{\varphi,M}^-, \delta z_{\varphi,M}^-) \quad \forall \Phi \in X_k^0.
\end{aligned} \tag{37}$$

Then (36) becomes

$$\begin{aligned}
0 = & \sum_{m=1}^{M-1} \left( J''_{\mathbf{u}\mathbf{u}}(q(t_m), \mathbf{u}(t_m))(\delta \mathbf{u}(t_m), \Phi(t_m)) \right. \\
& - a''_{\mathbf{u}\mathbf{u}}(q(t_m), \mathbf{u}(t_m))(\delta \mathbf{u}(t_m), \Phi(t_m), \mathbf{z}(t_m))\Delta t_m \\
& \left. - a'_{\mathbf{u}}(q(t_m), \mathbf{u}(t_m))(\Phi(t_m), \delta \mathbf{z}(t_m))\Delta t_m \right) \\
& + \sum_{m=1}^M \left( \gamma(\Phi_{\varphi, m-1}^-, \delta z_{\varphi, m-1}^+ - \delta z_{\varphi, m-1}^-)_{\{\varphi_m^- > \varphi_{m-1}^-\}} \right. \\
& \quad \left. + \eta(\Phi_{\varphi, m-1}^-, \delta z_{\varphi, m-1}^+ - \delta z_{\varphi, m-1}^-) \right) \\
& - \eta_0(\Phi_{u, 0}^-, \delta z_{u, 0}^-) \quad \forall \Phi \in X_k^0.
\end{aligned} \tag{38}$$

In the final reformulation we shift the index of the second sum (jump-terms) and take out the terms corresponding to  $m = 0$

$$\begin{aligned}
0 = & \sum_{m=1}^{M-1} \left( J''_{\mathbf{u}\mathbf{u}}(q(t_m), \mathbf{u}(t_m))(\delta \mathbf{u}(t_m), \Phi(t_m)) \right. \\
& - a''_{\mathbf{u}\mathbf{u}}(q(t_m), \mathbf{u}(t_m))(\delta \mathbf{u}(t_m), \Phi(t_m), \mathbf{z}(t_m))\Delta t_m \\
& - a'_{\mathbf{u}}(q(t_m), \mathbf{u}(t_m))(\Phi(t_m), \delta \mathbf{z}(t_m))\Delta t_m \\
& + \gamma(\Phi_{\varphi, m}^-, \delta z_{\varphi, m}^+ - \delta z_{\varphi, m}^-)_{\{\varphi_{m+1}^- > \varphi_m^-\}} \\
& \left. + \eta(\Phi_{\varphi, m}^-, \delta z_{\varphi, m}^+ - \delta z_{\varphi, m}^-) \right) \\
& + \gamma(\Phi_{\varphi, 0}^-, \delta z_{\varphi, 0}^+ - \delta z_{\varphi, 0}^-)_{\{\varphi_1^- > \varphi_0^-\}} + \eta(\Phi_{\varphi, 0}^-, \delta z_{\varphi, 0}^+ - \delta z_{\varphi, 0}^-) \\
& - \eta_0(\Phi_{u, 0}^-, \delta z_{u, 0}^-) \quad \forall \Phi \in X_k^0.
\end{aligned} \tag{39}$$

As already pointed out in the time-stepping scheme for the adjoint equation, all dual equations have to be solved backwards in time. Therefore, we solve the following equation for  $m = M - 1, M - 2, \dots, 1$

$$\begin{aligned}
0 = & J''_{\mathbf{u}\mathbf{u}}(q(t_m), \mathbf{u}(t_m))(\delta \mathbf{u}(t_m), \Phi(t_m)) \\
& - a''_{\mathbf{u}\mathbf{u}}(q(t_m), \mathbf{u}(t_m))(\delta \mathbf{u}(t_m), \Phi(t_m), \mathbf{z}(t_m))\Delta t_m \\
& - a'_{\mathbf{u}}(q(t_m), \mathbf{u}(t_m))(\Phi(t_m), \delta \mathbf{z}(t_m))\Delta t_m \\
& + \gamma(\Phi_{\varphi, m}^-, \delta z_{\varphi, m}^+ - \delta z_{\varphi, m}^-)_{\{\varphi_{m+1}^- > \varphi_m^-\}} \\
& + \eta(\Phi_{\varphi, m}^-, \delta z_{\varphi, m}^+ - \delta z_{\varphi, m}^-) \quad \forall \Phi \in X_k^0.
\end{aligned}$$

As a result, the only remaning terms in (39) are

$$\gamma(\Phi_{\varphi, 0}^-, \delta z_{\varphi, 0}^+ - \delta z_{\varphi, 0}^-)_{\{\varphi_1^- > \varphi_0^-\}} + \eta(\Phi_{\varphi, 0}^-, \delta z_{\varphi, 0}^+ - \delta z_{\varphi, 0}^-) - \eta_0(\Phi_{u, 0}^-, \delta z_{u, 0}^-). \tag{40}$$

Finally we can apply the assumption  $\eta_0 \ll \eta$  once more and drop the last term in (40). Consequently the following equations have to be solved for all  $\Phi \in X_k^0$ :

$$\begin{aligned}
(\Phi_{\varphi, 0}^-, \delta z_{\varphi, 0}^-) &= (\Phi_{\varphi, 0}^-, \delta z_{\varphi, 1}^-), \\
(\Phi_{u, 0}^-, \delta z_{u, 0}^-) &= (\Phi_{u, 0}^-, \delta z_{u, 1}^-).
\end{aligned}$$

Note that Remark 4.3 was applied to (40) as well.



## 4.7 Final complete algorithm

Gathering the optimization problem statement and the space-time discretizations from the previous sections and resulting time-stepping schemes for the four equations yields the complete method given in Algorithm 1.

## 5 Numerical studies

In this section we present six numerical experiments. In these experiments we use the tracking type functional of (10) to find an optimal control force that approximately produces a desired phase-field. All numerical computations are performed with the open source software libraries `deal.II` [5, 6] and `DOP-ELIB` [23, 28].

Since a large body of the published literature deals with forward phase-field fracture in which cracks propagate through large parts of the domain or even until domain boundaries, we emphasize that on purpose, short fractures are considered in our optimal control settings only. Specifically,  $\varphi_d$  is prescribed sufficiently small such that we clearly can distinguish between our optimal control final fractures and classical non-controlled fractures.

### 5.1 Experiment 1: horizontal fracture in right half domain

The first experiment is motivated by a standard problem: the single edge notched tension test [45, 44]. Here we consider the square domain  $\Omega = (0, 1)^2$  with a horizontal notch, see Fig. 1. The notch is in the middle of the right side of the domain, defined as  $(0.5, 1) \times \{0.5\}$ . The boundary  $\partial\Omega$  is partitioned as  $\partial\Omega = \Gamma_N \cup \Gamma_D \cup \Gamma_{\text{free}}$ , where  $\Gamma_N := [0, 1] \times \{1\}$ ,  $\Gamma_D := [0, 1] \times \{0\}$ , and  $\Gamma_{\text{free}} := \{0, 1\} \times (0, 1)$ . On  $\Gamma_N$  we apply the force  $q$  in orthogonal direction to the domain, on  $\Gamma_D$  we enforce homogeneous Dirichlet boundary conditions for the displacement  $u = 0$ , and on  $\Gamma_{\text{free}}$  we set homogeneous Neumann boundary conditions. We choose the time interval  $[0, 1]$  with 41 equidistant time points  $t_m$ , i.e.,  $T = 1$  and  $M = 40$ . The discrete control space  $Q_h$  is one-dimensional in the sense that the force is constant in time and is only applied in  $y$  direction. The spatial mesh consists of  $64 \times 64$  square elements, hence the element diameter is  $h = \sqrt{2}/64 \approx 0.0221$ . The initial values are given by  $\mathbf{u}_0 = (u_0, \varphi_0)$  where  $\varphi_0$  describes the horizontal notch:

$$\varphi_0(x, y) := \begin{cases} 0, & x \in (0.50, 1.00) \text{ and } y = 0.5, \\ 1, & \text{else.} \end{cases}$$

The desired phase-field  $\varphi_d$  is defined as a continuation of the initial notch to the left hand side of the domain, see  $\varphi_d^0$  in Fig. 1. In order to investigate the effect of  $\varphi_d$  on the optimal solution, we will use two different homotopy approaches. In approach (a) we will successively increase the length of the desired phase-field, and in approach (b) we will successively reduce the Tikhonov parameter  $\alpha$ . In both cases the motivation is to increase the weight of the physically motivated term  $\frac{1}{2}\|\varphi - \varphi_d\|^2$  in relation to the Tikhonov term. We will perform as many homotopy steps as possible, solving one NLP per step. The common nominal parameters used in both approaches are given in Table 1.

---

**Algorithm 1:** Overall space-time phase-field fracture control algorithm

---

**Data:** Domain  $\Omega$ , mesh  $\mathcal{T}_h$ , number of time intervals  $M$ , parameters  $\varepsilon, \kappa, G_c, \mu, \lambda, \gamma, \eta, \alpha$ , initial value  $\mathbf{u}_0$ , initial control guess  $q^0$ .

**Result:** Optimal control  $q$  and admissible solution  $\mathbf{u}$ .

1: Set  $k = 0$  and  $q^k = q^0$  and solve the state equation for  $\mathbf{u}$ :  $\mathcal{L}'_{\mathbf{z}}(q^k, \mathbf{u}, \mathbf{z})(\Phi) = 0 \ \forall \Phi$ .

Specifically, obtain  $\mathbf{u}(t_0)$  from (6) and then  $\mathbf{u}(t_1), \dots, \mathbf{u}(t_M)$  from (7);

2: Solve the adjoint equation for  $\mathbf{z}$ :  $\mathcal{L}'_{\mathbf{u}}(q^k, \mathbf{u}, \mathbf{z})(\Phi) = 0 \ \forall \Phi$ . Obtain  $\mathbf{z}(t_M)$  from (23), then  $\mathbf{z}(t_{M-1}), \dots, \mathbf{z}(t_1)$  from (25), and finally  $\mathbf{z}(t_0)$  from (26);

3: Construct the coefficient vector  $\mathbf{f} \in \mathbb{R}^n$  for the reduced gradient  $\nabla j(q^k)$  by solving

$\mathbf{G}\mathbf{f} = [j'(q^k)(q_i)]_{i=1}^n$ . Here  $q_i$  denotes the  $i$ -th basis function of the discrete control space  $Q_h$  and  $\mathbf{G}_{ij} = (q_i, q_j)$  defines the mass matrix. The derivatives  $j'(q^k)(q_i)$  for the right hand side are computed from the representation (17);

**while**  $\|\mathbf{f}\|_2 > TOL$  **do**

4: Obtain  $\delta q$  from the Newton equation,  $j''(q^k)(\delta q, q_i) = -j'(q^k)(q_i) \ \forall q_i$ , by minimizing  $m(q^k, \mathbf{d}) = j(q^k) + \langle \mathbf{f}, \mathbf{d} \rangle + \frac{1}{2} \langle \mathbf{H}\mathbf{d}, \mathbf{d} \rangle$  for a vector  $\mathbf{d} \in \mathbb{R}^n$  using the CG-method (matrix free). Here  $\mathbf{H} \in \mathbb{R}^{n \times n}$  denotes the coefficient matrix of  $\nabla^2 j(q^k)\delta q$ ;

**for every CG step do**

5: Solve the tangent equation for  $\delta \mathbf{u}$ :

$\mathcal{L}''_{q\mathbf{z}}(q^k, \mathbf{u}, \mathbf{z})(\delta q, \Phi) + \mathcal{L}''_{\mathbf{u}\mathbf{z}}(q^k, \mathbf{u}, \mathbf{z})(\delta \mathbf{u}, \Phi) = 0 \ \forall \Phi$ . Obtain  $\delta \mathbf{u}(t_0)$  from (31) and then  $\delta \mathbf{u}(t_1), \dots, \delta \mathbf{u}(t_M)$  from (32);

6: Solve the adjoint Hessian equation for  $\delta \mathbf{z}$ :

$\mathcal{L}''_{q\mathbf{u}}(q^k, \mathbf{u}, \mathbf{z})(\delta q, \Phi) + \mathcal{L}''_{\mathbf{u}\mathbf{u}}(q^k, \mathbf{u}, \mathbf{z})(\delta \mathbf{u}, \Phi) + \mathcal{L}''_{\mathbf{z}\mathbf{u}}(q^k, \mathbf{u}, \mathbf{z})(\delta \mathbf{z}, \Phi) = 0 \ \forall \Phi$ . Obtain  $\delta \mathbf{z}(t_M)$  from (37), then  $\delta \mathbf{z}(t_{M-1}), \dots, \delta \mathbf{z}(t_1)$  from (38), and finally  $\delta \mathbf{z}(t_0)$  from (39);

7: Construct the coefficient vector  $\mathbf{h} \in \mathbb{R}^n$  for  $\nabla^2 j(q^k)\delta q$  by solving

$\mathbf{G}\mathbf{h} = j''(q^k)(\delta q, q_i)_{i=1}^n$ , where  $j''(q^k)(\delta q, q_i)$  is represented via (17);

**end**

8: Choose a step length  $\nu$  by an Armijo backtracking method;

9: Set  $q^{k+1} = q^k + \nu \delta q$ ;

10: Repeat steps 1, 2, 3 for the new control  $q^{k+1}$  to obtain  $\mathbf{f}$  for  $\nabla j(q^{k+1})$ ;

11: Increment  $k = k + 1$ ;

**end**

---

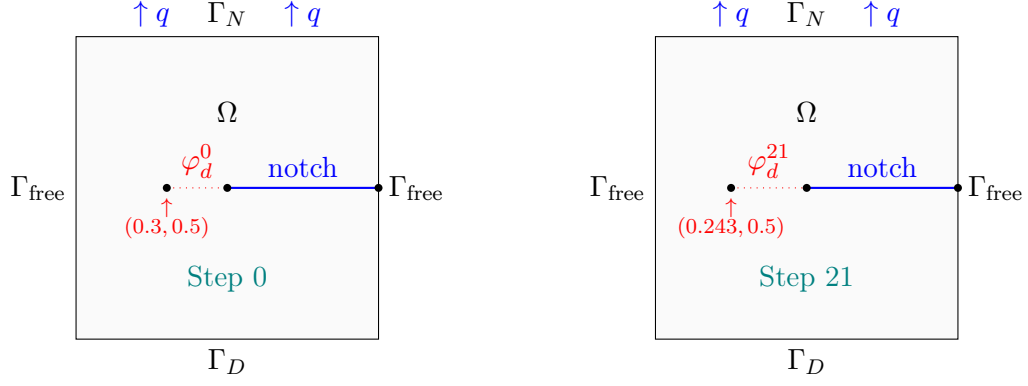


Figure 1: Experiment 1: domain  $\Omega = (0, 1)^2$  with partitioned boundary  $\partial\Omega$ , initial notch and desired crack  $\varphi_d$  for homotopy steps 0 and 21 in approach (a).

Table 1: Experiment 1: regularization and penalty parameters (left), model and material parameters (right).

Par.	Definition	Value	Par.	Definition	Value
$\varepsilon$	Regul. (crack) $\approx 4h$	0.0884	$G_c$	Fracture toughness	1.0
$\kappa$	Regul. (crack)	1.00e-10	$\nu_s$	Poisson's ratio	0.2
$\eta$	Regul. (viscosity)	1.00e3	$E$	Young's modulus	1.0e6
$\gamma$	Penalty	1.00e5	$q_0$	Initial control	1.0
$\alpha$	Tikhonov	4.75e-10	$q_d$	Nominal control	1.0e3

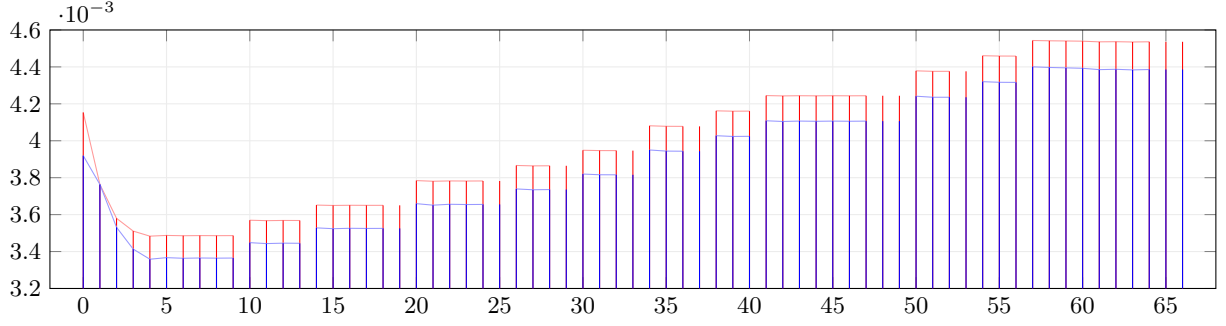


Figure 2: Experiment 1a: cost functional of each NLP iteration in homotopy (blue: tracking part above  $3.2\text{e-}3$  + red: Tikhonov part).

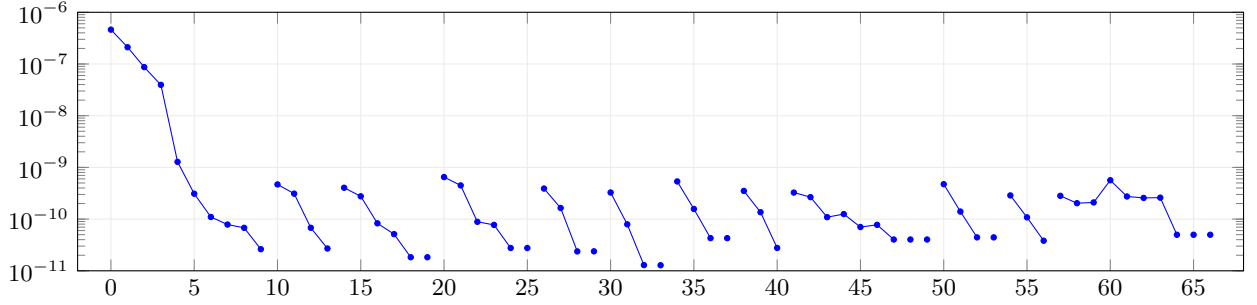


Figure 3: Experiment 1a: absolute residual of each NLP iteration in homotopy.

### 5.1.1 Approach (a): length increment

Here we will solve the NLP (10) several times with different desired phase-fields  $\varphi_d^k$ . Formally we define a sequence of desired phase-fields  $\varphi_d^k$  with  $\varphi_d^{k+1} < \varphi_d^k$  where  $\varphi_d^k$  is defined as

$$\varphi_d^k(x, y) := \begin{cases} 0, & x \in (0.3 \times 0.99^k, 0.5) \text{ and } y \in (0.5 - h, 0.5 + h), \\ 1, & \text{else.} \end{cases}$$

By this definition of  $\varphi_d^k$  we extend the desired crack to the left so that it becomes gradually longer. The number of homotopy steps performed in this experiment is 21: in step 22, the iterative solution of the nonlinear state equation fails because the Newton residuals do not decrease towards zero. Probably this means that large numerical errors prevent finding a descent direction or that the initial estimate lies outside the area of convergence, but various other reasons might be possible as well. Our results are presented in Table 2. The first column (Step) counts the homotopy steps. The second column (Iter) gives the number of Newton iterations for solving the associated reduced problem (11), except that Iter 0 in Step 0 refers to the initial guess from which the homotopy starts. The remaining values are the absolute Newton residual, the cost functional  $\mathcal{J}$  and its tracking part  $\frac{1}{2} \sum_m \|\varphi(t_m) - \varphi_d(t_m)\|^2$ , the maximal force  $|q_{\max}|$  applied on  $\Gamma_N$ , and the Tikhonov regularization term,  $\frac{\alpha}{2} \sum_m \|q(t_m) - q_d(t_m)\|_{\Gamma_N}^2$ . All values are rounded to three, five, or six significant digits. For every NLP the Newton iteration terminates when the residual falls below the tolerance  $5\text{e-}11$ .

Table 2: Experiment 1a: number of Newton iterations, absolute residual, cost terms and maximal force during homotopy. Iter 0 in step 0 refers to initial state from which homotopy starts.

Step	Iter	Residual	Cost	Tracking	Tikhonov	Force
0	0	4.62e−7	4.1532e−3	3.9192e−3	2.3406e−4	1.0
0	9	2.62e−11	3.4863e−3	3.3648e−3	1.2150e−4	2379.02
1	3	2.70e−11	3.5681e−3	3.4447e−3	1.2337e−4	2388.20
2	4	1.83e−11	3.6503e−3	3.5254e−3	1.2489e−4	2395.58
3	0	1.83e−11	3.6503e−3	3.5254e−3	1.2489e−4	2395.58
4	4	2.76e−11	3.7823e−3	3.6552e−3	1.2708e−4	2405.78
5	0	2.76e−11	3.7822e−3	3.6552e−3	1.2708e−4	2405.78
6	2	2.37e−11	3.8645e−3	3.7357e−3	1.2883e−4	2414.00
7	0	2.38e−11	3.8645e−3	3.7357e−3	1.2883e−4	2414.00
8	2	1.29e−11	3.9466e−3	3.8156e−3	1.3099e−4	2424.06
9	0	1.28e−11	3.9466e−3	3.8156e−3	1.3099e−4	2424.06
10	2	4.28e−11	4.0779e−3	3.9433e−3	1.3465e−4	2439.95
11	0	4.28e−11	4.0779e−3	3.9433e−3	1.3465e−4	2439.95
12	2	2.77e−11	4.1605e−3	4.0241e−3	1.3640e−4	2447.20
13	6	4.03e−11	4.2438e−3	4.1063e−3	1.3748e−4	2451.38
14	0	4.03e−11	4.2438e−3	4.1063e−3	1.3748e−4	2451.38
15	0	4.03e−11	4.2438e−3	4.1063e−3	1.3748e−4	2451.38
16	2	4.43e−11	4.3760e−3	4.2356e−3	1.4043e−4	2464.78
17	0	4.43e−11	4.3760e−3	4.2356e−3	1.4043e−4	2464.78
18	2	3.82e−11	4.4585e−3	4.3160e−3	1.4258e−4	2472.69
19	7	4.98e−11	4.5360e−3	4.3858e−3	1.5012e−4	2498.67
20	0	4.98e−11	4.5360e−3	4.3858e−3	1.5012e−4	2498.67
21	0	4.98e−11	4.5360e−3	4.3858e−3	1.5012e−4	2498.67

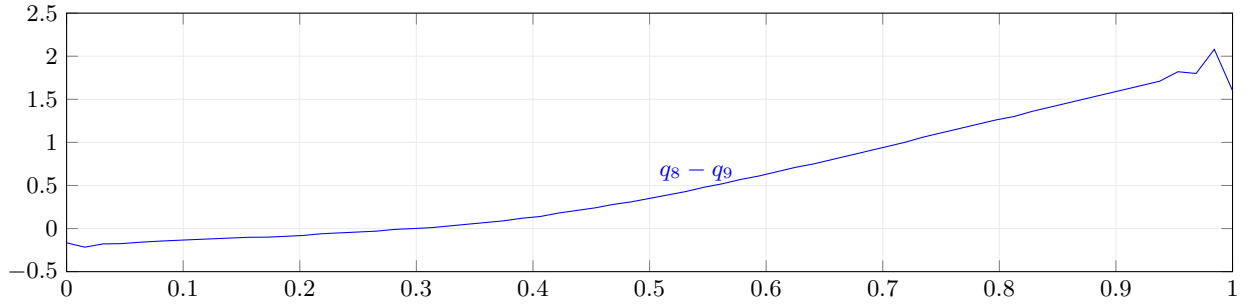


Figure 4: Experiment 1b: difference of control forces on iterations 8 and 9 in homotopy step 0.

### 5.1.2 Approach (b): Tikhonov iteration

The second approach is a successive reduction of  $\alpha$ , a so called Tikhonov iteration. In this case the length of the desired phase-field remains constant at  $\varphi_d^0$  for all homotopy steps while the weight of the Tikhonov term in  $\mathcal{J}$  is successively reduced. Here we define the sequence by  $\alpha_k = 0.99^k \alpha_0$  with  $\alpha_0 = 4.75\text{e-}10$ . The number of homotopy steps performed is 8: in step 9, we have terminated the computation because of very slow alternating convergence of the residual as is often observed for very small values of the parameter  $\alpha$ . The results are presented in Table 3. First we notice the high sensitivity of our NLP solution with respect to the control force. In Fig. 4 we present the difference of the controls on iterations 8 and 9 of the initial homotopy step. A comparison of the corresponding residuals shows a reduction from  $6.78\text{e-}11$  to  $2.62\text{e-}11$  (approximately 60%), even though the maximal difference between the applied controls is only 2.1 (or 0.1%). The values of the cost functional and the residual on all iterations of both homotopies are presented in Figs. 2, 3, 5 and 6. Each dot in Fig. 3 stands for one Newton step within the corresponding homotopy iteration. The behavior of the residual values in both approaches is typical for homotopy methods: in each homotopy step they are reduced below the tolerance, and they increase slightly afterwards. In the final homotopy step of each approach the reduction is non-monotonous because the maximal number of line search iterations is reached; this indicates the difficulty of the NLP. In Fig. 2 we observe that the value of the cost functional increases with each homotopy step. This is a consequence of the increasing length of the desired phase-field:  $\varphi_d^{21} < \dots < \varphi_d^0$ . A closer look at the results reveals that the tracking part actually increases non-linearly with the length of the desired phase-field, which is not surprising as our overall problem is nonlinear. Finally we observe that both approaches yield larger maximal control forces when compared to the results without homotopy ansatz. In approach (a) the maximal final control is 2498.67, and in approach (b) it is 2438.79. This corresponds to the different cracks being produced: without any homotopy approach the crack has a total length of 0.063, with the Tikhonov iteration (approach b) we obtain 0.078, and with the crack length increment (approach a) we obtain 0.094; see Fig. 7. We notice that we do not infer from these results any evaluation on which approach is better for this test case, but we can only say that both yield different findings.

Table 3: Experiment 1b: number of Newton iterations, absolute residual, cost terms and maximal force during homotopy. Iter 0 in step 0 refers to initial state from which homotopy starts.

Step	Iter	Residual	Cost	Tracking	Tikhonov	Force
0	0	4.62e-7	4.1532e-3	3.9192e-3	2.3406e-4	1.0
0	9	2.62e-11	3.4863e-3	3.3648e-3	1.2150e-4	2379.02
1	3	4.47e-11	3.4835e-3	3.3614e-3	1.2206e-4	2387.69
2	4	1.55e-11	3.4812e-3	3.3590e-3	1.2212e-4	2393.56
3	6	2.20e-11	3.4787e-3	3.3565e-3	1.2223e-4	2399.79
4	6	2.81e-11	3.4764e-3	3.3541e-3	1.2226e-4	2405.43
5	2	2.81e-11	3.4737e-3	3.3512e-3	1.2257e-4	2412.03
6	3	3.88e-11	3.4706e-3	3.3469e-3	1.2362e-4	2423.04
7	2	2.42e-11	3.4676e-3	3.3433e-3	1.2437e-4	2432.00
8	6	4.79e-11	3.4648e-3	3.3310e-3	1.2487e-4	2438.79

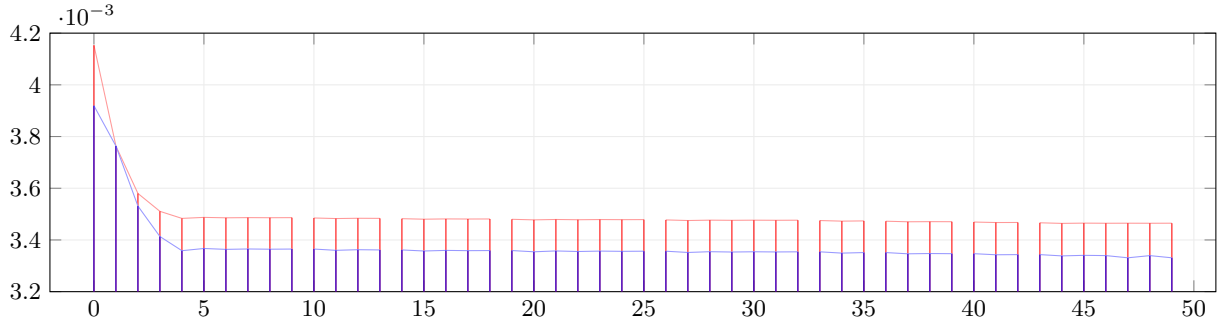


Figure 5: Experiment 1b: cost functional of each NLP iteration in homotopy (blue: tracking part above  $3.2e-3$  + red: Tikhonov part).

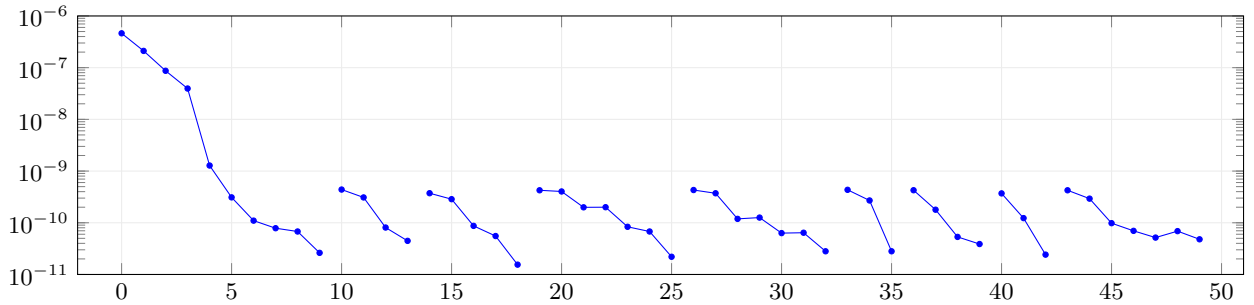


Figure 6: Experiment 1b: absolute residual of each NLP iteration in homotopy.

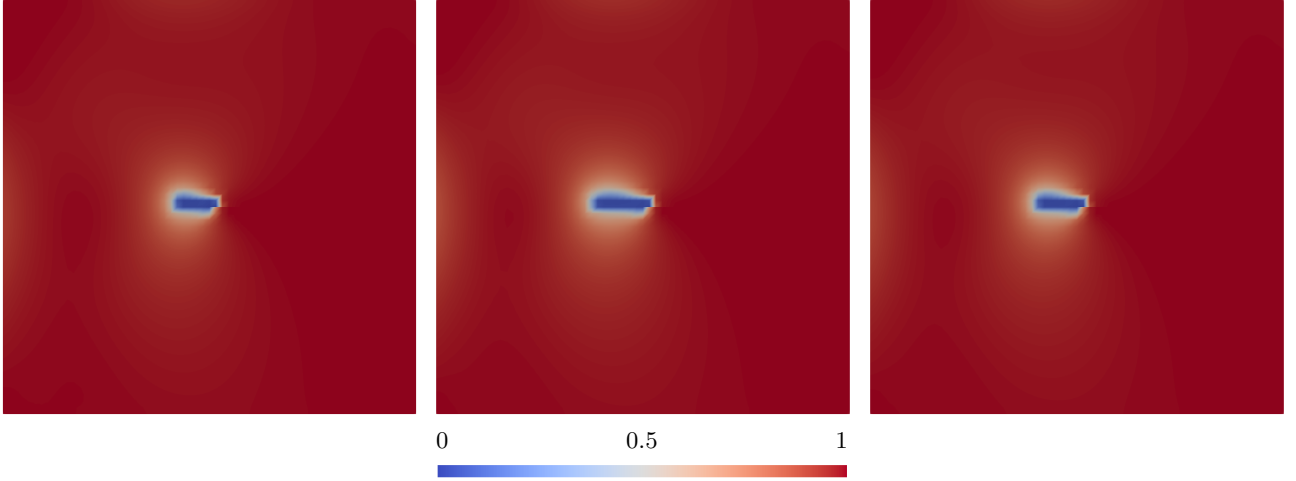


Figure 7: Experiment 1: optimal phase-field  $\varphi$  at time 40. Step 0 (left), step 19 of approach (a) (center, best result), step 8 of approach (b) (right).

## 5.2 Experiment 2: two-sided control for diagonal crack

Our second experiment is an extension of the first one with the aim to create a crack that grows diagonally, in negative  $x$  direction and positive  $y$  direction. We consider the same domain as before,  $\Omega = (0, 1)^2$ , but since cracks grow orthogonal to the maximum tensile stress [65, Chapter 4], the original control boundary  $\Gamma_N = [0, 1] \times \{1\}$  becomes  $\Gamma_{N_1}$  and we extend the control to a second boundary  $\Gamma_{N_2} = \{0\} \times [0, 1]$ , i.e., in the PDE constraint, we have

$$(q, \Phi_{u:\perp})_{\Gamma_N, I} = (q, \Phi_{u:y})_{\Gamma_{N_1}, I} + (q, \Phi_{u:x})_{\Gamma_{N_2}, I}.$$

The overall setting is shown in Fig. 8. Because of the second control boundary, the Tikhonov term in the cost functional now becomes an integral over the union  $\Gamma_N := \Gamma_{N_1} \cup \Gamma_{N_2}$ . The domain is partitioned into  $128 \times 128$  square elements with diameter  $h = \sqrt{2}/128$ . The number of time steps is  $M = 100$ . The desired phase-field is given as

$$\varphi_d(x, y) := \begin{cases} 0, & x \in (0.1, 0.5) \text{ and } |y - (0.85 - 0.7x)| \leq 3h, \\ 1, & \text{else.} \end{cases}$$

In short, the desired crack goes diagonally from  $(0.5, 0.5)$  to  $(0.1, 0.78)$  with a vertical diameter of  $6h$ . The results are presented in Table 4 and Figs. 9 to 11. From Table 4 we can see that it takes 13 iterations to solve the NLP with an absolute tolerance of  $2.0\text{e}-10$ . Note that from now on the first two columns (Iter, CG) give the iteration index of Newton's method on the reduced NLP and the number of CG iterations required for computing the Newton increment, respectively. The Newton iteration terminates when either the relative or the absolute residual falls below the requested tolerance. The cost functional is reduced from  $4.47\text{e}-2$  to  $1.28\text{e}-2$ , by approximately 70%. The final phase-field is shown in Fig. 9. As one can clearly see, the desired diagonal crack propagation has been produced successfully. On the one hand, the crack has to propagate to the left, therefore the control on the upper boundary  $\Gamma_{N_1}$  has to increase from left to right. On the other hand, the crack should propagate upwards, therefore the control on the left boundary  $\Gamma_{N_2}$  has to decrease from bottom to top. In



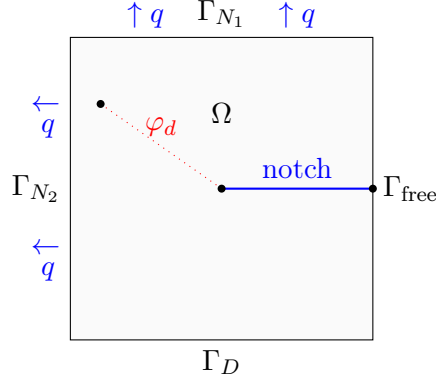


Figure 8: Experiment 2: domain  $\Omega = (0, 1)^2$  with partitioned boundary, initial notch and desired crack  $\varphi_d$ .

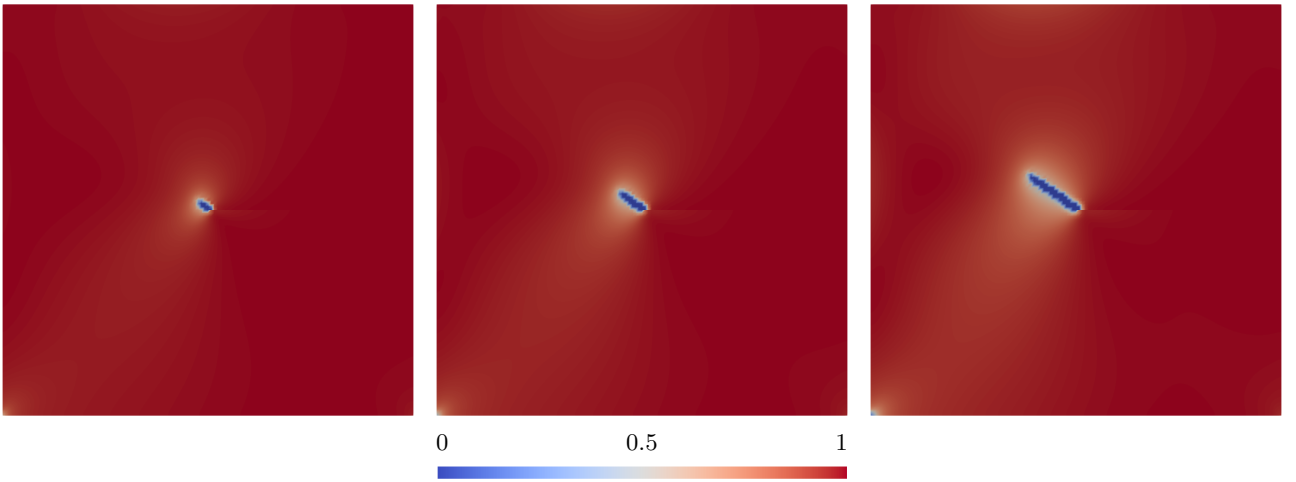


Figure 9: Experiment 2: optimal phase-field  $\varphi$  at times 50, 75, and 100.

contrast to Experiment 1, no symmetry in the displacement or adjoints fields can be expected since here the notch is horizontal whereas the desired phase-field is diagonal. Note that Fig. 11 shows a kink in each control. This is a numerical artefact: at the cell in the top left corner, the control acts on two adjacent boundaries simultaneously, and the discretized quantities interact within this single cell. In Fig. 9 we finally notice a tiny crack propagation starting from the bottom left edge  $(0, 0)$ . This is due to the singularity caused by the Dirichlet condition on the bottom boundary  $\Gamma_D$  in combination with the control acting as Neumann condition on  $\Gamma_{N_2}$ . Similar observations are made in Section 5.5.

### 5.3 Experiment 3: connecting horizontal cracks for a sliced domain

Our third experiment is motivated by a simple question: Is it possible to connect some (but not all) notches in a given domain? Here we consider the rectangle  $\Omega = (0, 2.2) \times (0, 0.4)$  with four horizontal notches  $\mathcal{N}_1 := (0.3, 0.5) \times \{0.2\}$ ,  $\mathcal{N}_2 := (0.7, 0.9) \times \{0.2\}$ ,  $\mathcal{N}_3 := (1.3, 1.5) \times \{0.2\}$ ,  $\mathcal{N}_4 := (1.7, 1.9) \times \{0.2\}$ , see Fig. 12. This yields the combined notch  $\mathcal{N} := \bigcup_{i=1}^4 \mathcal{N}_i$  with initial phase-field

$$\varphi_0(x, y) := \begin{cases} 0, & (x, y) \in \mathcal{N}, \\ 1, & \text{else.} \end{cases}$$

Table 4: Experiment 2: number of CG iterations, residuals, cost terms and maximal force during NLP iteration.

Iter	CG	Relative residual	Absolute residual	Cost	Tracking	Tikhonov	Force
0	–	1.0	1.99e−5	4.4742e−2	1.3723e−2	3.1019e−2	10
1	2	3.70e−3	7.36e−8	1.3075e−2	1.3075e−2	8.9902e−9	2202.36
2	9	1.27e−3	2.52e−8	1.2879e−2	1.2824e−2	5.4707e−5	2443.45
3	6	5.77e−4	1.15e−8	1.2818e−2	1.2719e−2	9.8469e−5	2525.62
4	5	3.11e−4	6.20e−9	1.2790e−2	1.2667e−2	1.2261e−4	2565.05
5	4	1.84e−4	3.67e−9	1.2775e−2	1.2638e−2	1.3678e−4	2584.23
6	4	1.13e−4	2.26e−9	1.2766e−2	1.2620e−2	1.4553e−4	2596.34
7	3	7.57e−5	1.51e−9	1.2760e−2	1.2609e−2	1.5102e−4	2605.50
8	2	4.86e−5	9.67e−10	1.2756e−2	1.2602e−2	1.5474e−4	2609.38
9	3	3.53e−5	7.03e−10	1.2754e−2	1.2597e−2	1.5710e−4	2613.69
10	2	2.42e−5	4.82e−10	1.2752e−2	1.2593e−2	1.5886e−4	2614.90
11	2	1.55e−5	3.09e−10	1.2751e−2	1.2591e−2	1.6008e−4	2616.43
12	2	1.01e−5	2.01e−10	1.2750e−2	1.2589e−2	1.6086e−4	2617.60
13	2	6.81e−6	1.36e−10	1.2750e−2	1.2588e−2	1.6138e−4	2618.43

Table 5: Experiment 2: regularization and penalty parameters (left), model and material parameters (right).

Par.	Definition	Value	Par.	Definition	Value
$\varepsilon$	Regul. (crack) $\approx 4h$	0.0442	$G_c$	Fracture toughness	1.0
$\kappa$	Regul. (crack)	1.0e−10	$\nu_s$	Poisson’s ratio	0.2
$\eta$	Regul. (viscosity)	1.0e3	$E$	Young’s modulus	1.0e6
$\gamma$	Penalty	1.0e5	$q_0$	Initial control	10.0
$\alpha$	Tikhonov	6.5e−9	$q_d$	Nominal control	2.2e3

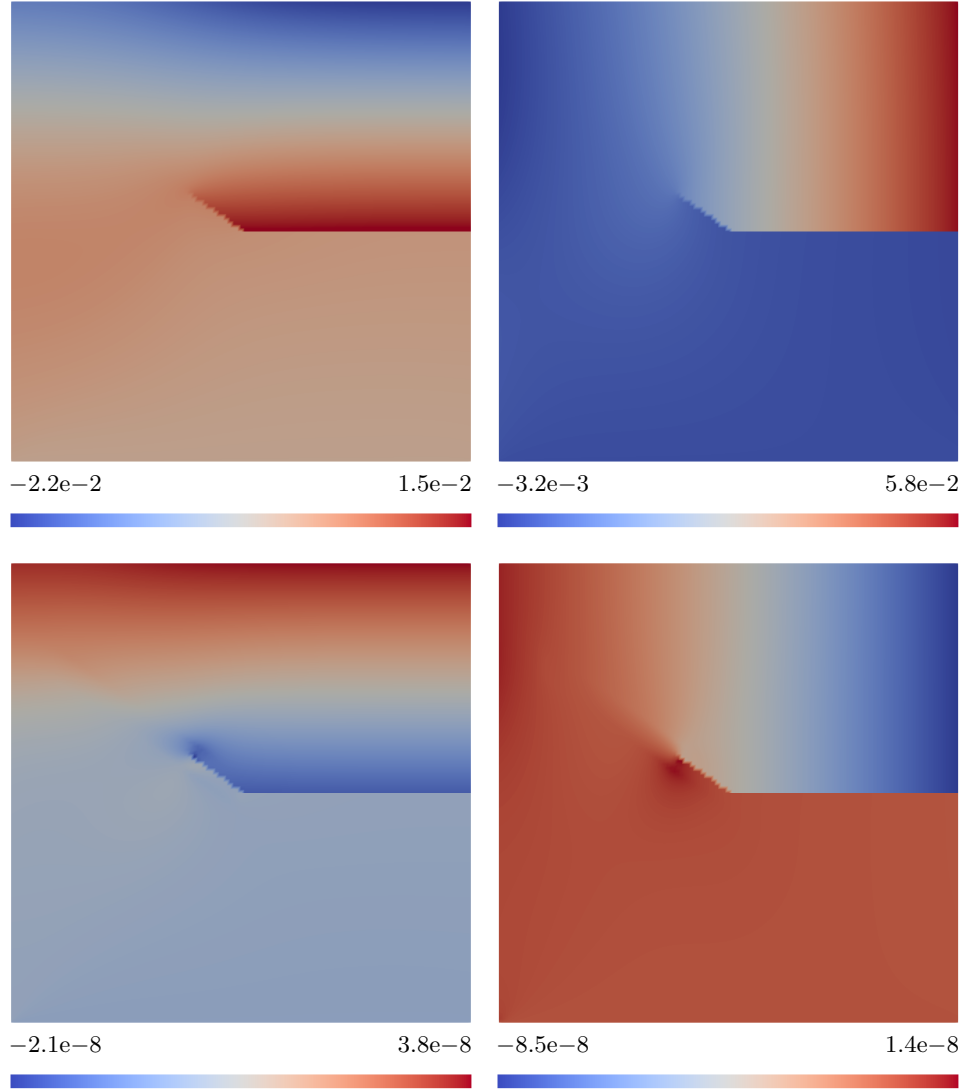


Figure 10: Experiment 2: optimal displacement field  $u$  (top:  $x$  left,  $y$  right) and adjoint field  $z_u$  (bottom:  $x$  left,  $y$  right) at time 250.

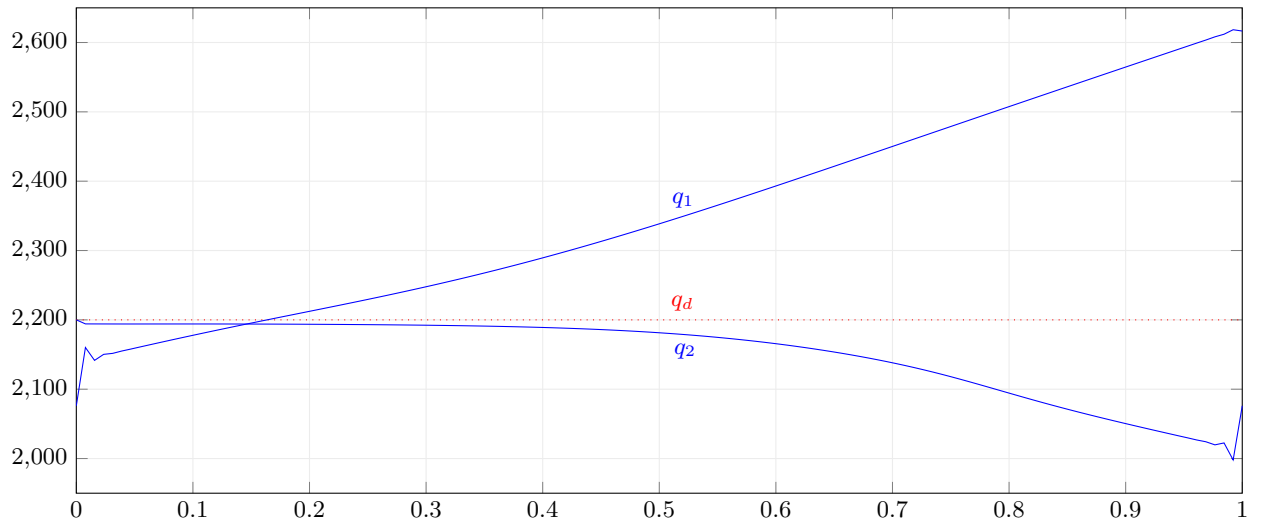


Figure 11: Experiment 2: optimal control forces (solid:  $q_1$  on upper boundary  $\Gamma_{N_1}$ ,  $q_2$  on left boundary  $\Gamma_{N_2}$ ) and common nominal control force  $q_d$  (dotted).

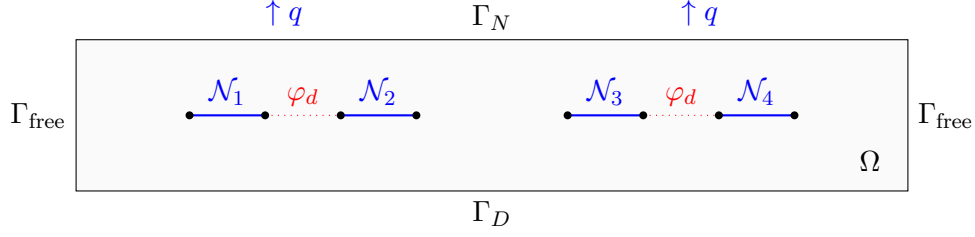


Figure 12: Experiment 3: domain  $\Omega = (0, 2.2) \times (0, 0.4)$  with partitioned boundary  $\partial\Omega$ , initial notches  $\mathcal{N}_1, \dots, \mathcal{N}_4$ , and desired cracks  $\varphi_d$ .

Table 6: Experiment 3: regularization and penalty parameters (left), model and material parameters (right).

Par.	Definition	Value	Par.	Definition	Value
$\varepsilon$	Regul. (crack) $\approx 4h$	0.035	$G_c$	Fracture toughness	1.0
$\kappa$	Regul. (crack)	1.0e-10	$\nu_s$	Poisson's ratio	0.2
$\eta$	Regul. (viscosity)	1.0e3	$E$	Young's modulus	1.00e6
$\gamma$	Penalty	1.0e5	$q_0$	Initial control	1.0
$\alpha$	Tikhonov	2.1e-10	$q_d$	Nominal control	6.53e3

The boundary  $\partial\Omega$  is partitioned as in Section 5.1. The time interval is again  $[0, 1]$  but with 2001 equidistant time points, i.e.,  $T = 1$  and  $M = 2000$ . The spatial mesh now consists of  $352 \times 64$  square elements with diameter  $h = \sqrt{2} \times 0.4/64 \approx 0.00884$ . The desired phase-field  $\varphi_d$  connects  $\mathcal{N}_1$  with  $\mathcal{N}_2$  and  $\mathcal{N}_3$  with  $\mathcal{N}_4$ , hence it is defined as follows:

$$\varphi_d(x, y) := \begin{cases} 0, & x \in (0.5, 0.7) \cup (1.5, 1.7) \text{ and } y \in (0.2 - 4h, 0.2 + 4h), \\ 1, & \text{else.} \end{cases}$$

All relevant parameters for this experiment are presented in Table 6. The results for the tolerance  $2.0\text{e-}9$  are shown in Table 7. From the final optimal phase-field in Fig. 13 (bottom) we see that the desired phase-field has indeed been reached, since  $\mathcal{N}_1$  is connected with  $\mathcal{N}_2$  and  $\mathcal{N}_3$  with  $\mathcal{N}_4$ . The optimal control force shown in Fig. 16 is rather strong and has two roughly parabolic maxima right at the two sections where notches are to be connected, which is to be expected from a mechanical point of view. The four cracks propagating from both ends of each pair of connected notches, where no cracks are desired, can be explained by the decreasing control at the end points. That decreasing control generates a different principal axis of tension which in turn produces the non-horizontal crack growth. In Fig. 15 (top) we present the optimal displacement fields at time step 2000. They are both symmetric and reach their maxima right at the two sections where notches are to be connected. This is consistent with the behavior of the control forces and again physically plausible. For comparison, before the middle cracks join, we also display the respective fields at time step 1800 in Fig. 14.

Table 7: Experiment 3: number of CG iterations, residuals, cost terms and maximal force during NLP iteration.

Iter	CG	Relative residual	Absolute residual	Cost	Tracking	Tikhonov	Force
0	–	1.0	2.00e–6	2.3850e–2	1.4302e–2	9.5483e–3	100.00
1	2	0.110	2.20e–7	1.2839e–2	1.2839e–2	3.4223e–8	6550.69
2	2	3.13e–2	6.27e–8	1.2428e–2	1.2309e–2	1.1897e–4	7899.32
3	2	1.22e–2	2.44e–8	1.2330e–2	1.2139e–2	1.9136e–4	8264.47
4	2	9.34e–3	1.87e–8	1.2292e–2	1.2066e–2	2.2519e–4	8403.51
5	2	1.44e–3	2.89e–9	1.2263e–2	1.2011e–2	2.5205e–4	8501.55
6	2	9.20e–4	1.84e–9	1.2261e–2	1.2006e–2	2.5478e–4	8514.26

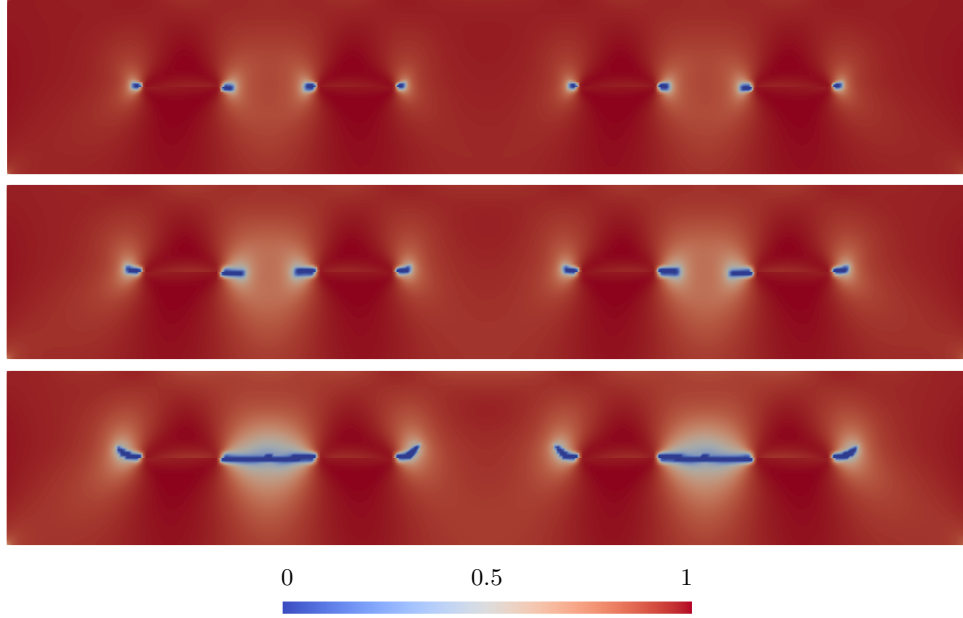


Figure 13: Experiment 3: optimal phase-field  $\varphi$  at times 1400, 1800, and 2000.

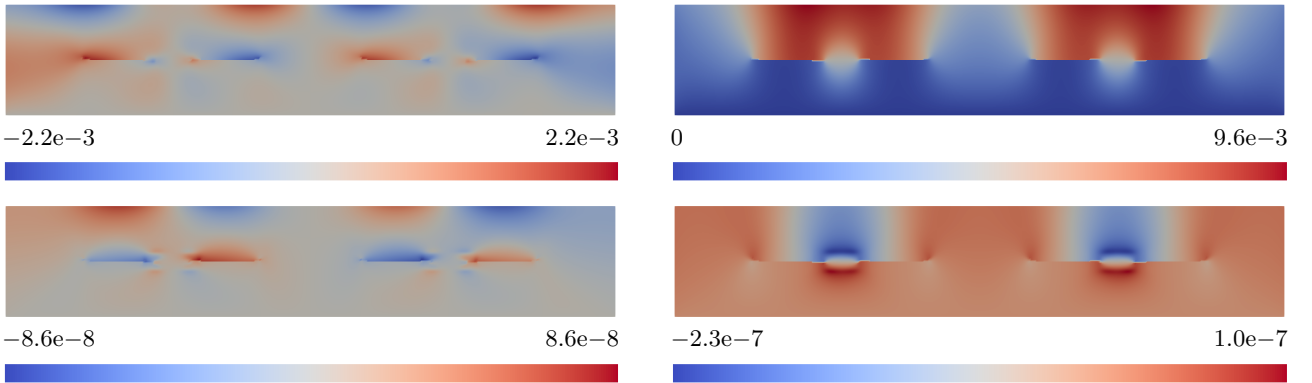


Figure 14: Experiment 3: optimal displacement field  $u$  (top:  $x$  left,  $y$  right) and adjoint field  $z_u$  (bottom:  $x$  left,  $y$  right) at time 1800.

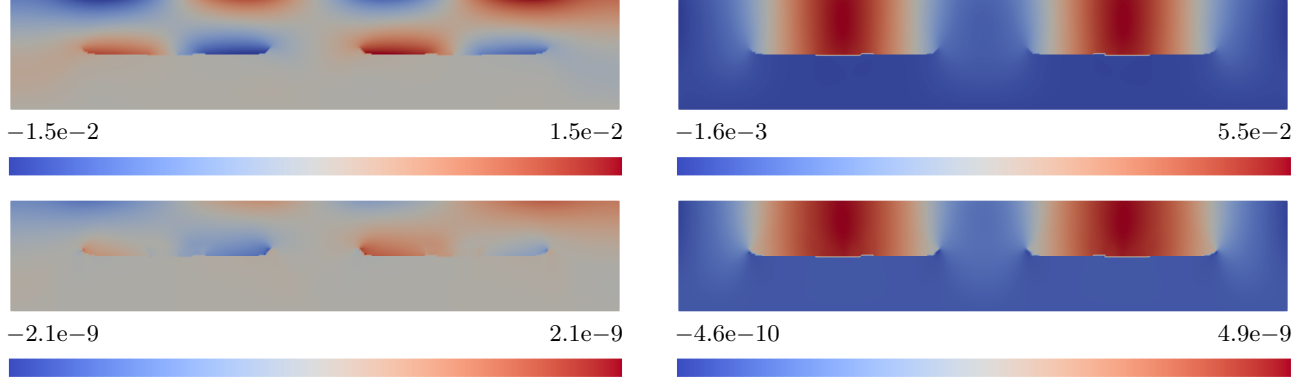


Figure 15: Experiment 3: optimal displacement field  $u$  (top:  $x$  left,  $y$  right) and adjoint field  $z_u$  (bottom:  $x$  left,  $y$  right) at time 2000.

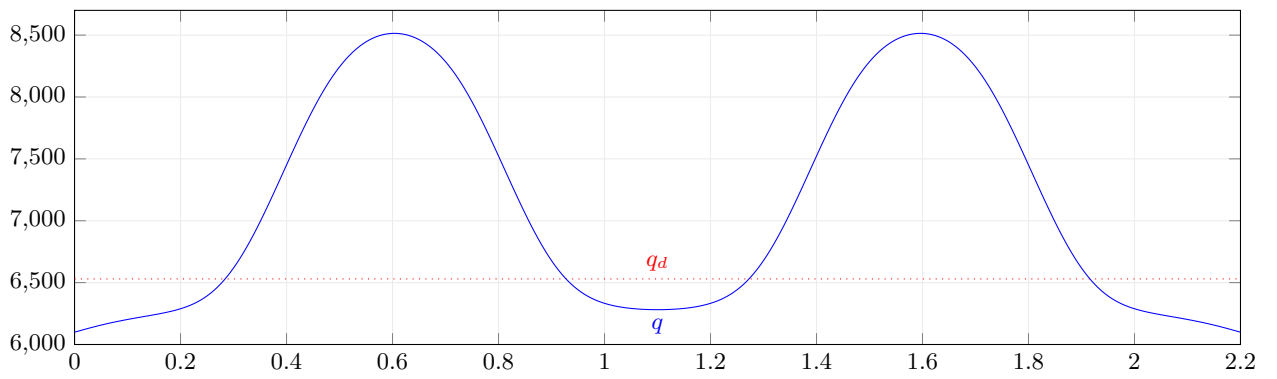


Figure 16: Experiment 3: optimal control force (solid) and nominal control force (dotted) on upper boundary  $\Gamma_N$ .

#### 5.4 Experiment 4: connecting two horizontal cracks for an entirely sliced domain

The fourth experiment is motivated by the question whether it is possible to connect two horizontal notches to achieve an entirely sliced domain. Here we consider again the square domain  $\Omega = (0, 1)^2$ , but now with two horizontal notches, see Fig. 17. The left notch is defined as  $(0.0, 0.375) \times \{0.5\}$ , the right notch is defined as  $(0.625, 1.0) \times \{0.5\}$ . The boundary  $\partial\Omega$  is partitioned as in Section 5.1. We choose the time interval  $[0, 1]$  with 251 equidistant time points, i.e.,  $T = 1$  and  $M = 250$ . The spatial mesh now consists of  $128 \times 128$  square elements with diameter  $h = \sqrt{2}/128 \approx 0.011$ . The desired phase-field  $\varphi_d$  connects the left notch with the right notch and is defined as follows:

$$\varphi_d(x, y) := \begin{cases} 0, & x \in (0.375, 0.625) \text{ and } y \in (0.5 - 2h, 0.5 + 2h), \\ 1, & \text{else.} \end{cases}$$

Our goal in this experiment is rather peculiar. Analytically, the PDE constraint becomes singular once the domain is entirely sliced. In the phase-field model this happens when the left and right boundaries of  $\Omega$  are connected by a path along which the phase-field  $\varphi$  vanishes. Numerical difficulties are to be expected even before such a path exists: the PDE becomes increasingly ill-conditioned when the transition zones with  $0 < \varphi < 1$  come into contact. Nevertheless it is possible to create a domain-splitting crack with a pure forward model, see for instance the related single edge notched tension test [45, 44, 2, 18]. Yet this experiment remains numerically difficult and becomes even more challenging within our optimization setting. Since we have to expect that the solution of the forward problem might be close to singularities, it is not clear what will happen when we insert this solution into the optimization algorithm. With regard to this challenge we have observed that in many experiments the Tikhonov term acts against extreme forces and improves the solvability of the PDE for the resulting controls. In the experiment under consideration we set  $\alpha$  to  $2.0\text{e-}10$ . By this the Tikhonov term is not the driving factor of the optimization process, but still large enough to avoid extreme forces. The choice of the other parameters is shown in Table 8, and our results are presented in Table 9 and Figs. 18 to 20.

In Table 9 we observe that the residual value is decreasing, except for the last iteration. After iteration 6 the PDE forward problem becomes unsolvable. Therefore we regard iteration 5 as the optimal solution: it has the lowest absolute residual value,  $5.13\text{e-}9$ , and also the lowest relative residual value,  $1.57\text{e-}2$ . The results presented in Table 9 and Figs. 18 to 20 refer to iteration 5. The optimal phase-field presented in Fig. 18 does not connect the two notches but reaches approximately two thirds of the length of the desired phase-field. In Fig. 20 we see that the optimal control force is nearly twice as large as the nominal control force  $q_d$ . This means that the optimization is primarily driven by the physical term  $\|\varphi - \varphi_d\|^2$ .

#### 5.5 Experiment 5: L-shaped domain

In our fifth experiment we study a modification of the L-shaped panel test within an optimization context. The L-shaped panel test was originally developed by Winkler [62] and extensively studied in [2, 43, 59, 41]. In the original test the applied force pushes upwards against a small left-most section

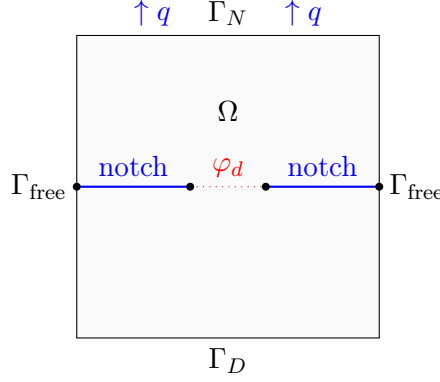


Figure 17: Experiment 4: domain  $\Omega = (0,1)^2$  with partitioned boundary  $\partial\Omega$ , initial notches, and desired crack  $\varphi_d$ .

Table 8: Experiment 4: regularization and penalty parameters (left), model and material parameters (right).

Par.	Definition	Value	Par.	Definition	Value
$\varepsilon$	Regul. (crack) $\approx 2h$	0.0221	$G_c$	Fracture toughness	1.0
$\kappa$	Regul. (crack)	1.0e-10	$\nu_s$	Poisson's ratio	0.2
$\eta$	Regul. (viscosity)	1.0e3	$E$	Young's modulus	1.00e6
$\gamma$	Penalty	1.0e5	$q_0$	Initial control	1.0
$\alpha$	Tikhonov	2.0e-10	$q_d$	Nominal control	1.85e3

Table 9: Experiment 4: number of CG iterations, residuals, cost terms and maximal force during NLP iteration.

Iter	CG	Relative residual	Absolute residual	Cost	Tracking	Tikhonov	Force
0	–	1.0	3.26e-7	5.5093e-3	5.2936e-3	2.1566e-4	380.0
1	2	0.424	1.38e-7	4.9612e-3	4.9584e-3	2.7903e-6	2043.40
2	3	0.238	7.75e-8	4.7486e-3	4.6748e-3	7.3883e-5	2845.85
3	3	0.145	4.72e-8	4.6179e-3	4.4620e-3	1.5592e-4	3300.68
4	3	4.54e-2	1.48e-8	4.5391e-3	4.3184e-3	2.2067e-4	3573.22
5	2	1.57e-2	5.13e-9	4.5160e-3	4.2733e-3	2.4274e-4	3629.90
6	2	0.26	8.36e-8	4.5088e-3	4.2591e-3	2.4976e-4	3632.82



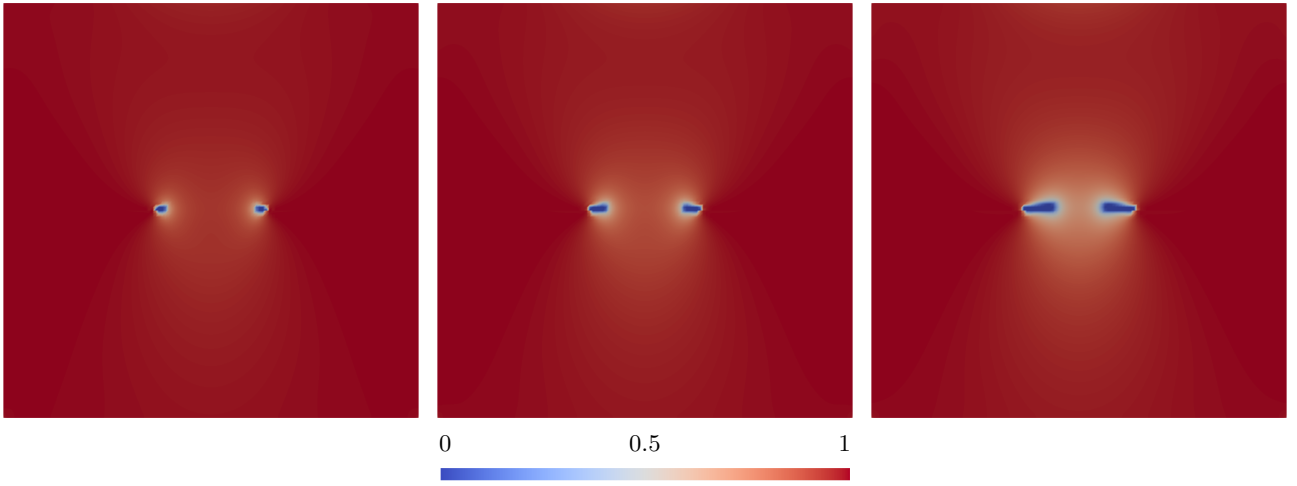


Figure 18: Experiment 4: optimal phase-field  $\varphi$  at times 150, 200, and 250.

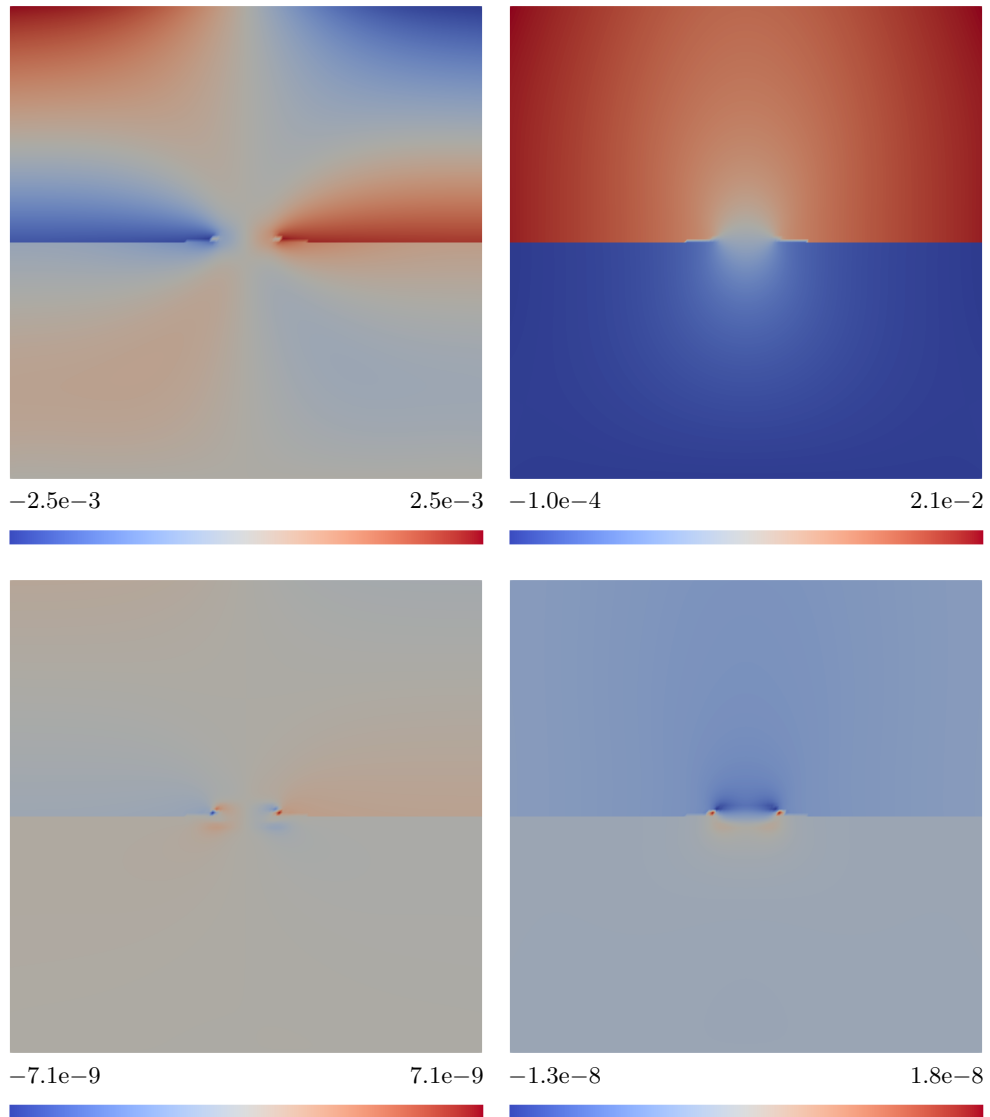


Figure 19: Experiment 4: optimal displacement field  $u$  (top:  $x$  left,  $y$  right) and adjoint field  $z_u$  (bottom:  $x$  left,  $y$  right) at time 250.

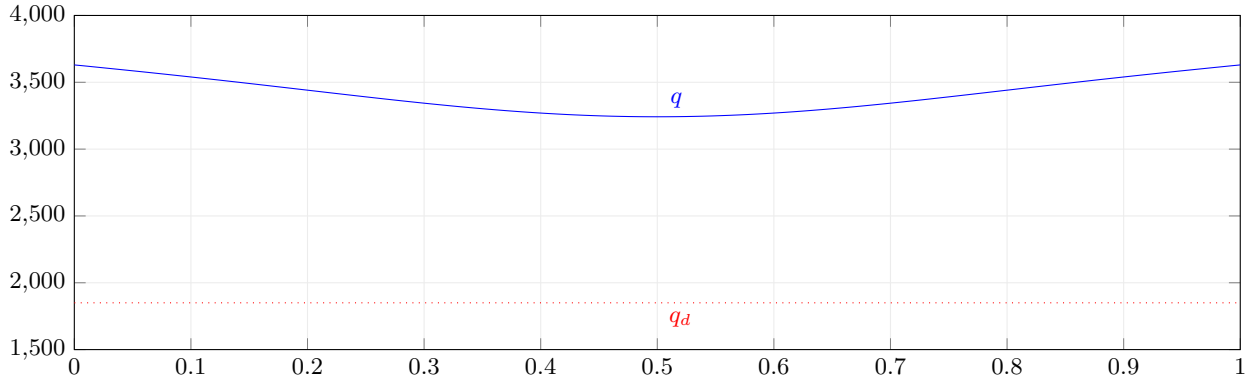


Figure 20: Experiment 4: optimal control force (solid) and nominal control force (dotted) on upper boundary  $\Gamma_N$ .

of the upper part of the domain. In our experiment we apply a pulling force on the top boundary  $\Gamma_N$  instead. We do this in order to have a complete control boundary within the optimization context. The L-shaped domain  $\Omega = (0, 1)^2 \setminus (0.5, 0.5)^2$  and its partitioning of the boundary  $\partial\Omega$  are shown in Fig. 21. We choose the time interval  $[0, 1]$  with 301 equidistant time points, i.e.,  $T = 1$  and  $M = 300$ . Each of the  $3 \times 80 \times 80$  square spatial mesh elements has a diameter of  $h = \sqrt{2}/160 \approx 0.00884$ . All other parameters are shown in Table 10. From [2, 43, 59, 41] and [62] we already know that the crack will grow slightly above the horizontal line  $[0.5, 1] \times \{0.5\}$ . Therefore we place the desired phase-field  $\varphi_d$  also slightly above that line,

$$\varphi_d(x, y) := \begin{cases} 0, & x \in (0.5, 1.0) \text{ and } y \in (0.53 - 4h, 0.53 + 4h), \\ 1, & \text{else.} \end{cases}$$

We are aware that a fracture with this phase-field cannot be produced in our setting for two reasons. First, a sharp crack along  $[0.5, 1.0] \times \{0.53\}$  is physically impossible because the crack will always start to grow from the singularity in  $(0.5, 0.5)$ . Second, a decomposition of the stress tensor is needed in order to distinguish crack growth under tension and compression; see extensive findings and discussions for the L-shaped panel test in [2]. Since stress splitting laws introduce further nonlinearities in the forward phase-field fracture model and do not contribute to significant further insight in the current work, we have not used them, despite implemented in our software, e.g., [41]. We also tried to define  $\varphi_d$  on the horizontal line  $[0.5, 1] \times \{0.5\}$ . However, since the crack starts propagating diagonally upwards from  $(0.5, 0.5)$ , the values of the residual and the cost functional did not decrease, and as a consequence the Newton iteration for the optimization problem did not converge. Our results for the tolerance  $2.0\text{e}-10$  are presented in Table 11 and Figs. 22 to 24.

In Table 11 we see that 24 iterations were required to reach the final residual value  $1.89\text{e}-10$ . The propagating crack, shown in Fig. 22, is very similar to the results from [41]. The corresponding optimal control is presented in Fig. 24. It decreases almost linearly, approximately from 2400 to 1500, which is plausible since this experiment has similarities to Section 5.1. Similar to Section 5.2 we notice a small crack propagation starting from the lower left corner  $(0.5, 0)$ . This is due to the singularity caused by the Dirichlet condition on  $\Gamma_D$  in combination with the Neumann condition on  $\{0.5\} \times [0, 0.5]$ .

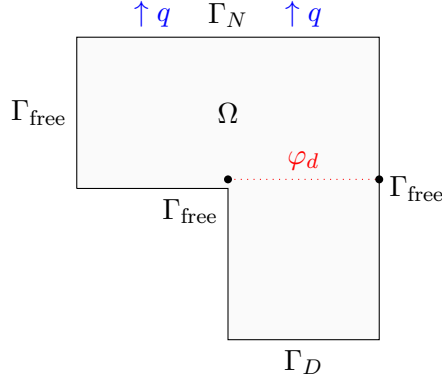


Figure 21: Experiment 5: L-shaped domain  $\Omega = (0, 1)^2 \setminus (0.5, 0.5)^2$  with partitioned boundary and desired crack  $\varphi_d$ .

Table 10: Experiment 5: regularization and penalty parameters (left), model and material parameters (right).

Par.	Definition	Value	Par.	Definition	Value
$\varepsilon$	Regul. (crack) $\approx 4h$	0.0354	$G_c$	Fracture toughness	1.0
$\kappa$	Regul. (crack)	1.000e-10	$\nu_s$	Poisson's ratio	0.2
$\eta$	Regul. (viscosity)	1.000e3	$E$	Young's modulus	1.0e6
$\gamma$	Penalty	1.000e5	$q_0$	Initial control	1.0
$\alpha$	Tikhonov	2.625e-9	$q_d$	Nominal control	1.6e3

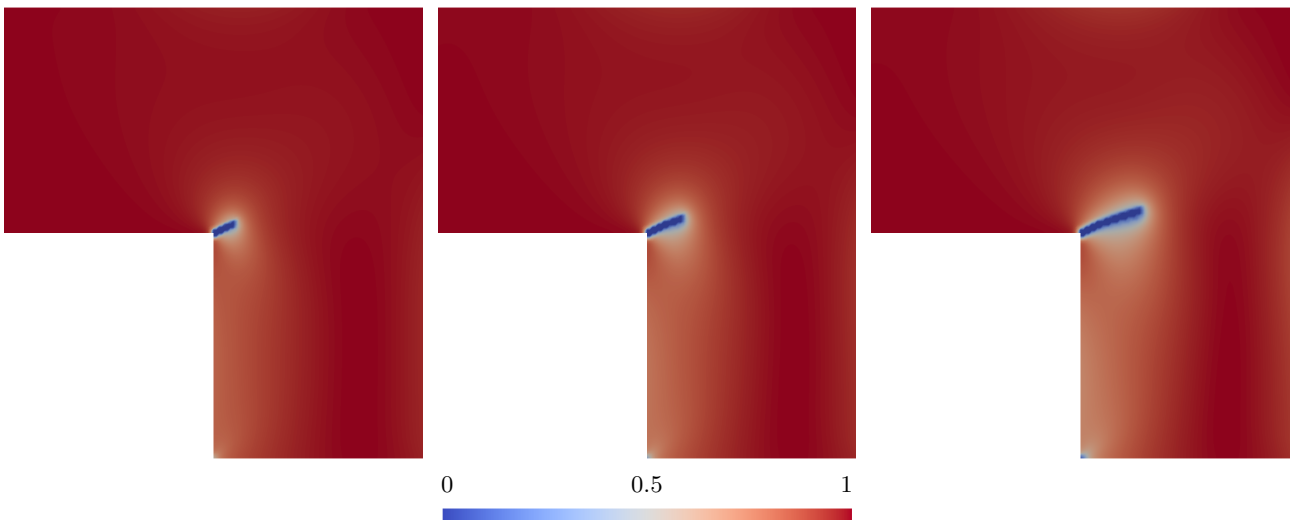


Figure 22: Experiment 5: optimal phase-field  $\varphi$  at times 200, 250, and 300.

Table 11: Experiment 5: number of CG iterations, residuals, cost terms and maximal force during NLP iteration.

Iter	CG	Relative residual	Absolute residual	Cost	Tracking	Tikhonov	Force
0	–	1.0	4.34e–6	2.0637e–2	8.9261e–3	1.1711e–2	1.0
1	2	0.117	5.09e–7	1.6652e–2	8.8773e–3	7.7750e–3	1600.27
2	2	4.71e–2	2.04e–7	1.6473e–2	8.9092e–3	7.5637e–3	1982.44
3	3	2.45e–2	1.06e–7	1.6404e–2	8.9210e–3	7.4829e–3	2143.55
4	2	1.18e–3	5.11e–9	1.6367e–2	8.9284e–3	7.4387e–3	2226.13
5	3	7.86e–4	3.41e–9	1.6344e–2	8.9340e–3	7.4103e–3	2279.40
6	4	5.85e–4	2.54e–9	1.6329e–2	8.9382e–3	7.3905e–3	2304.63
7	3	4.33e–4	1.88e–9	1.6317e–2	8.9419e–3	7.3750e–3	2334.29
8	3	3.37e–4	1.46e–9	1.6308e–2	8.9450e–3	7.3630e–3	2350.53
9	2	2.68e–4	1.16e–9	1.6301e–2	8.9478e–3	7.3534e–3	2360.71
10	3	2.20e–4	9.56e–10	1.6296e–2	8.9501e–3	7.3455e–3	2374.60
11	2	1.84e–4	7.96e–10	1.6291e–2	8.9521e–3	7.3388e–3	2380.56
12	2	1.58e–4	6.83e–10	1.6287e–2	8.9539e–3	7.3331e–3	2387.88
13	2	1.36e–4	5.92e–10	1.6284e–2	8.9555e–3	7.3281e–3	2394.83
14	3	1.20e–4	5.21e–10	1.6281e–2	8.9569e–3	7.3239e–3	2401.26
15	2	1.03e–4	4.46e–10	1.6278e–2	8.9583e–3	7.3200e–3	2403.82
16	2	9.21e–5	4.00e–10	1.6276e–2	8.9594e–3	7.3166e–3	2407.58
17	2	8.23e–5	3.57e–10	1.6274e–2	8.9605e–3	7.3135e–3	2411.42
18	2	7.45e–5	3.23e–10	1.6272e–2	8.9615e–3	7.3107e–3	2415.00
19	2	6.83e–5	2.96e–10	1.6271e–2	8.9624e–3	7.3082e–3	2418.35
20	2	6.17e–5	2.68e–10	1.6269e–2	8.9633e–3	7.3058e–3	2421.39
21	2	5.84e–5	2.53e–10	1.6268e–2	8.9640e–3	7.3037e–3	2424.17
22	2	5.31e–5	2.30e–10	1.6266e–2	8.9648e–3	7.3016e–3	2426.76
23	2	4.82e–5	2.09e–10	1.6265e–2	8.9658e–3	7.2997e–3	2429.09
24	2	4.35e–5	1.89e–10	1.6264e–2	8.9661e–3	7.2980e–3	2431.26

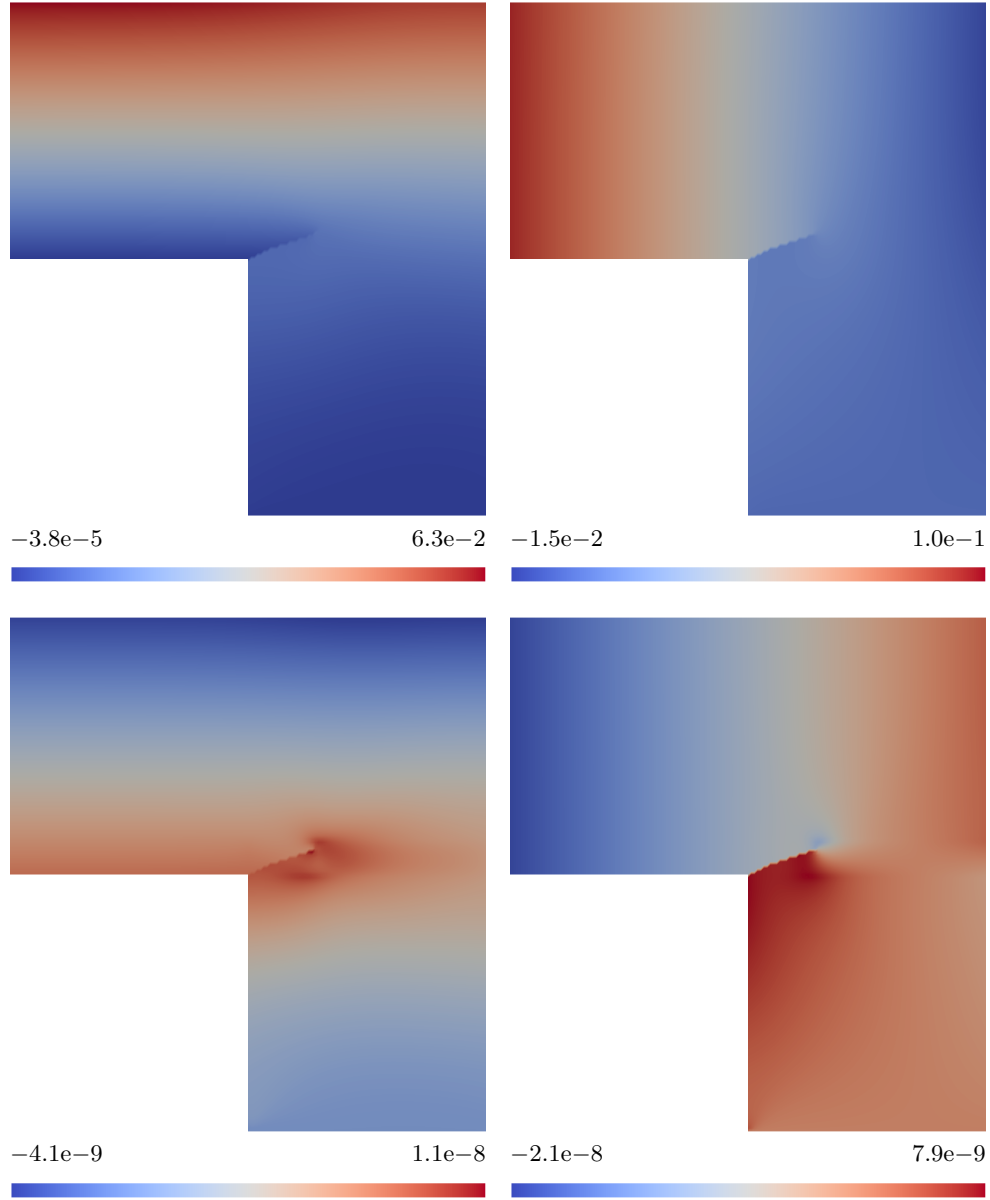


Figure 23: Experiment 5: optimal displacement field  $u$  (top:  $x$  left,  $y$  right) and adjoint field  $z_u$  (bottom:  $x$  left,  $y$  right) at time 300.

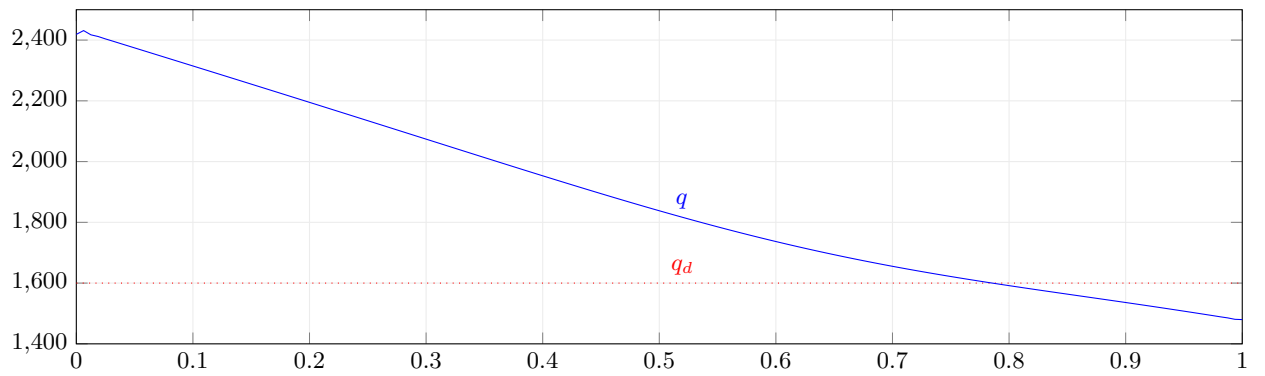


Figure 24: Experiment 5: optimal control force (solid) and nominal control force (dotted) on upper boundary  $\Gamma_N$ .

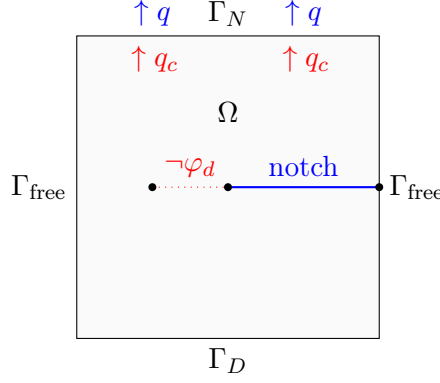


Figure 25: Experiment 6: domain  $\Omega = (0, 1)^2$  with partitioned boundary, initial notch, undesired crack  $\neg\varphi_d$  and constant pulling force  $q_c$ .

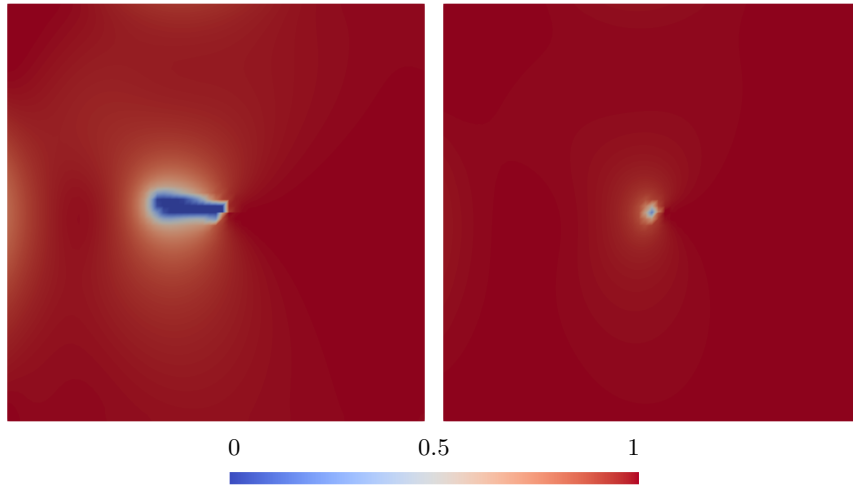


Figure 26: Experiment 6: initial phase-field  $\varphi$  (left, iteration 0) and optimal phase-field (right, iteration 15) at final time 100.

## 5.6 Experiment 6: inhibiting horizontal crack growth

In our final experiment we expose the domain  $\Omega = (0, 1)^2$  to a time-independent external force  $q_c$  which creates a growing crack (for the tiny initial control  $q = 1$ ). Then we seek an optimal control  $q$  that counteracts the external force  $q_c$  to inhibit the crack growth. We choose the same partitioning of  $\partial\Omega$  and the same notch as in Section 5.1. The initial phase-field is

$$\varphi_0(x, y) := \begin{cases} 0, & x \in (0.5, 1) \text{ and } y = 0.5 \\ 1, & \text{else.} \end{cases}$$

We define the external force as a linear function:  $q_c(x) = 850 + 1800x$ . The time interval is  $[0, 1]$  with 101 equidistant time points, i.e.,  $T = 1$  and  $M = 100$ . The spatial mesh consists of  $64 \times 64$  square elements with diameter  $h = \sqrt{2}/64$ . The desired phase-field  $\varphi_d$  has the value one on the whole domain. Our findings for the tolerance  $2.0\text{e-}11$  are presented in Table 12 and Figs. 26 to 28.

In Fig. 26 we observe that no crack propagation occurs with the computed optimal control. As a result, the desired phase-field is successfully reproduced and the initial value of the cost functional is reduced by 96%. In comparison to all other experiments, where we achieved a maximum reduction of

Table 12: Experiment 6: number of CG iterations, residuals, cost terms and maximal force during NLP iteration.

Iter	CG	Relative residual	Absolute residual	Cost	Tracking	Tikhonov	Force
0	–	1.0	3.23e−6	1.7274e−3	1.4082e−3	3.1920e−4	1.0
1	3	0.558	1.80e−6	1.5649e−3	2.1034e−5	1.5438e−3	4262.61
2	3	0.166	5.38e−7	1.9198e−4	1.8984e−4	2.1348e−6	824.97
3	3	0.137	4.44e−7	1.2174e−4	7.6886e−6	1.1405e−4	1731.04
4	3	5.26e−2	1.70e−7	9.3561e−5	9.0843e−5	2.7177e−6	956.04
5	3	4.40e−2	1.42e−7	6.5026e−5	3.4897e−5	3.0129e−5	1280.33
6	3	1.25e−3	4.05e−9	7.2949e−5	6.3052e−5	9.8963e−6	1079.64
7	12	1.02e−3	3.31e−9	6.7607e−5	5.2538e−5	1.5069e−5	1142.82
8	12	3.10e−4	1.00e−9	7.0443e−5	5.8585e−5	1.1858e−5	1104.25
9	10	2.52e−4	8.16e−10	6.9141e−5	5.5993e−5	1.3148e−5	1120.23
10	9	7.94e−5	2.57e−10	6.9890e−5	5.7514e−5	1.2377e−5	1110.86
11	7	6.42e−5	2.07e−10	6.9560e−5	5.6853e−5	1.2707e−5	1114.79
12	7	2.03e−5	6.57e−11	6.9753e−5	5.7241e−5	1.2512e−5	1112.52
13	5	1.63e−5	5.28e−11	6.9669e−5	5.7073e−5	1.2596e−5	1113.45
14	4	5.26e−6	1.70e−11	6.9718e−5	5.7172e−5	1.2546e−5	1112.98
15	3	4.21e−6	1.36e−11	6.9697e−5	5.7128e−5	1.2568e−5	1113.14

Table 13: Experiment 6: regularization and penalty parameters (left), model and material parameters (right).

Par.	Definition	Value	Par.	Definition	Value
$\varepsilon$	Regul. (crack) $\approx 2h$	0.0442	$G_c$	Fracture toughness	1.0
$\kappa$	Regul. (crack)	1.0e−10	$\nu_s$	Poisson’s ratio	0.2
$\eta$	Regul. (viscosity)	1.0e3	$E$	Young’s modulus	1.0e6
$\gamma$	Penalty	1.0e5	$q_0$	Initial control	1.0
$\alpha$	Tikhonov	1.0e−9	$q_d$	Nominal control	−8.0e2

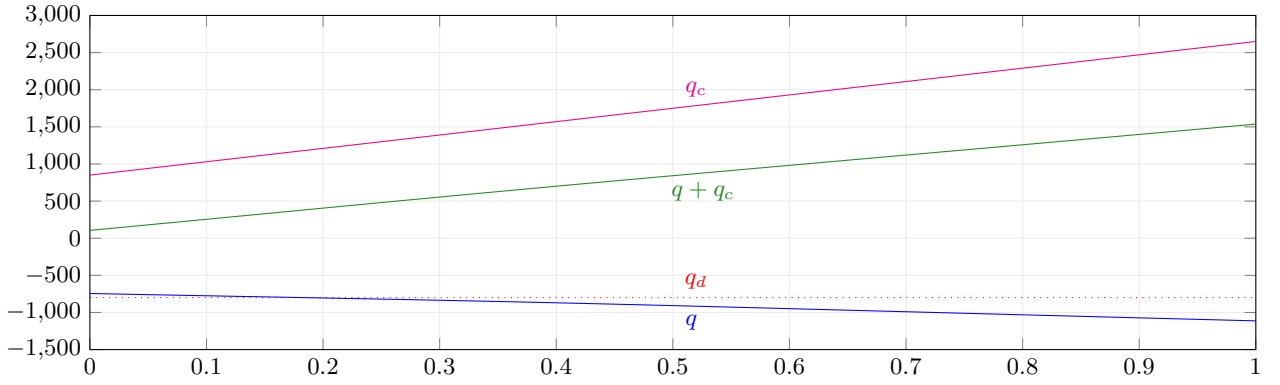


Figure 27: Experiment 6: optimal control force (blue), nominal control (red, dotted), constant control (magenta) and resulting total control  $q + q_c$  (green) on upper boundary  $\Gamma_N$ .

70%, this is a remarkable result. Although the sum of the optimal control  $q$  and the constant external force  $q_c$  is positive everywhere, see Fig. 27, it is not large enough to create a propagating crack. This is to be expected since the Tikhonov term would penalize an unnecessarily strong control force. In Fig. 28 the control forces of iterations 1 to 4 from Table 12 are shown. We observe that the first control  $q_1$  decreases almost linearly to a minimal value of  $-4262.61$ , which produces a relatively large Tikhonov term. The second control  $q_2$  is instead a linearly increasing function that minimizes this term. The third and fourth controls lie between  $q_1$  and  $q_2$ , and  $q_4$  behaves similar to the optimal control. When studying the value of the tracking part in Table 12, we observe that it becomes almost zero on the third iteration where the Tikhonov term is more than 10 times larger. Consequently the Tikhonov term must be reduced next. Subsequently, the two terms oscillate until they are roughly balanced. Some of the former experiments have been sensitive to the choice of  $\alpha$ , but none of them has been as sensitive as this experiment.

## 6 Conclusions

In this paper we derived a space-time Galerkin formulation for a regularized phase-field fracture optimal control setting. By introducing jump terms in time and with the help of a discontinuous Galerkin discretization in time, specific time-stepping schemes were obtained. A careful investigation of correct weighting of two regularization terms and the initial conditions was necessary for the forward phase-field fracture problem. The solution process of the optimization problem was based on the reduced approach in which the state variables are obtained from a solution operator acting on the controls. The numerical solution algorithm is based on Newton's method in which three auxiliary problems are required. The first part of the paper was concerned with the detailed derivation of these terms, which are to the best of our knowledge novel in the published literature.

In Section 5, we performed several detailed computational performance studies for space-time phase-field fracture optimal control problems. The optimization problem was designed with the help of a reduced approach in which the state variables are obtained from a solution operator acting on the controls. Therein, a monolithic space-time representation of the phase-field fracture problem



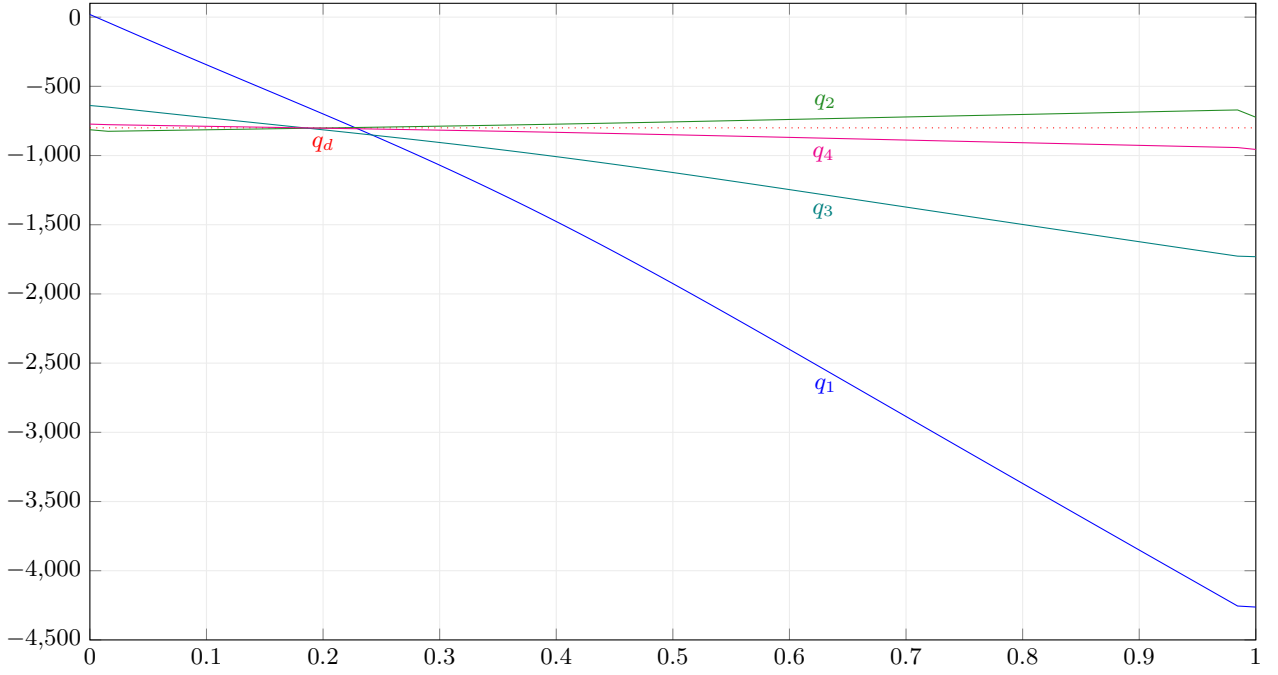


Figure 28: Experiment 6: control forces for iterations 1–4 (solid) and nominal control (dotted) on upper boundary  $\Gamma_N$ .

was adopted. Moreover, the crack irreversibility constraint was regularized using a penalty approach. To study the performance, we investigated six numerical experiments with single (Experiments 1, 2, 5, 6) and multiple fractures (Experiments 3, 4), single controls (Experiments 1, 3, 4, 5, 6) and two controls (Experiments 2), propagating fractures (Experiments 1, 2, 3, 4, 5) and inhibiting crack growth (Experiment 6). Therein, the performance of the NLP solver (Algorithm 1) and the inner CG method as well as the phase-field fracture PDE constraint were computationally analyzed in great detail. One main bottleneck is the computational cost of the inner linear solver of the forward problem, which is well-known and analogous in other PDE-constrained optimization problems. In ongoing work, we plan to incorporate parallel adaptive preconditioned iterative solvers [32, 33], which, however, is a major extension and was out of scope in this work.

## 7 Acknowledgements

The first and third author are partially funded by the Deutsche Forschungsgemeinschaft (DFG, German Research Foundation) Priority Program 1962 (DFG SPP 1962) within the subproject *Optimizing Fracture Propagation using a Phase-Field Approach* with the project number 314067056. The second author is funded by the DFG – SFB1463 – 434502799.

## References

- [1] G. Allaire, F. Jouve, and N. V. Goethem. Damage and fracture evolution in brittle materials by shape optimization methods. *Journal of Computational Physics*, 230(12):5010 – 5044, 2011.

- [2] M. Ambati, T. Gerasimov, and L. De Lorenzis. A review on phase-field models of brittle fracture and a new fast hybrid formulation. *Computational Mechanics*, 55(2):383–405, 2015.
- [3] L. Ambrosio and V. Tortorelli. Approximation of functionals depending on jumps by elliptic functionals via  $\gamma$ -convergence. *Comm. Pure Appl. Math.*, 43:999–1036, 1990.
- [4] L. Ambrosio and V. Tortorelli. On the approximation of free discontinuity problems. *Boll. Un. Mat. Ital. B*, 6:105–123, 1992.
- [5] D. Arndt, W. Bangerth, T. C. Clevenger, D. Davydov, M. Fehling, D. Garcia-Sanchez, G. Harper, T. Heister, L. Heltai, M. Kronbichler, R. M. Kynch, M. Maier, J.-P. Pelteret, B. Turcksin, and D. Wells. The `deal.II` library, version 9.1. *Journal of Numerical Mathematics*, 2019.
- [6] D. Arndt, W. Bangerth, D. Davydov, T. Heister, L. Heltai, M. Kronbichler, M. Maier, J.-P. Pelteret, B. Turcksin, and D. Wells. The `deal.II` finite element library: Design, features, and insights. *Computers & Mathematics with Applications*, 2020.
- [7] V. P. Barbu. *Optimal Control of Variational Inequalities*, volume 100. Pitman Advanced Pub. Program, 1984.
- [8] R. Becker, D. Meidner, and B. Vexler. Efficient numerical solution of parabolic optimization problems by finite element methods. *Optim. Methods Softw.*, 22(5):813–833, 2007.
- [9] P. Benner, A. Cohen, M. Ohlberger, and K. Willcox. *Model Reduction and Approximation: Theory and Algorithms*. SIAM Philadelphia, 2015.
- [10] M. J. Borden, C. V. Verhoosel, M. A. Scott, T. J. R. Hughes, and C. M. Landis. A phase-field description of dynamic brittle fracture. *Comput. Meth. Appl. Mech. Engrg.*, 217:77–95, 2012.
- [11] B. Bourdin. Image segmentation with a finite element method. *Mathematical Modelling and Numerical Analysis*, 33(2):229–244, 1999.
- [12] B. Bourdin. Numerical implementation of the variational formulation for quasi-static brittle fracture. *Interfaces and free boundaries*, 9:411–430, 2007.
- [13] B. Bourdin, G. Francfort, and J.-J. Marigo. Numerical experiments in revisited brittle fracture. *J. Mech. Phys. Solids*, 48(4):797–826, 2000.
- [14] B. Bourdin, G. Francfort, and J.-J. Marigo. The variational approach to fracture. *J. Elasticity*, 91(1–3):1–148, 2008.
- [15] B. Bourdin and G. A. Francfort. Past and present of variational fracture. *SIAM News*, 52(9), 2019.
- [16] B. Bourdin, C. Larsen, and C. Richardson. A time-discrete model for dynamic fracture based on crack regularization. *Int. J. Frac.*, 168(2):133–143, 2011.
- [17] A. Braides. *Approximation of free-discontinuity problems*. Springer Berlin Heidelberg, 1998.

- [18] M. K. Brun, T. Wick, I. Berre, J. M. Nordbotten, and F. A. Radu. An iterative staggered scheme for phase field brittle fracture propagation with stabilizing parameters. *Computer Methods in Applied Mechanics and Engineering*, 361:112752, 2020.
- [19] S. Burke, C. Ortner, and E. Süli. An adaptive finite element approximation of a variational model of brittle fracture. *SIAM J. Numer. Anal.*, 48(3):980–1012, 2010.
- [20] P. G. Ciarlet. *The Finite Element Method for Elliptic Problems*. North-Holland, Amsterdam [u.a.], 2. pr. edition, 1987.
- [21] J. Desai, G. Allaire, and F. Jouve. Topology optimization of structures undergoing brittle fracture. *Journal of Computational Physics*, 458:111048, 2022.
- [22] P. Diehl, R. Lipton, T. Wick, and M. Tyagi. A comparative review of peridynamics and phase-field models for engineering fracture mechanics. *Computational Mechanics*, pages 1–35, 2022.
- [23] The Differential Equation and Optimization Environment: DOPELIB.
- [24] G. Francfort. Variational fracture: Twenty years after. *International Journal of Fracture*, pages 1–11, 2021.
- [25] G. Francfort and J.-J. Marigo. Revisiting brittle fracture as an energy minimization problem. *J. Mech. Phys. Solids*, 46(8):1319–1342, 1998.
- [26] T. Gerasimov and L. D. Lorenzis. A line search assisted monolithic approach for phase-field computing of brittle fracture. *Computer Methods in Applied Mechanics and Engineering*, 312:276–303, 2016.
- [27] T. Gerasimov, U. Römer, J. Vondřejc, H. G. Matthies, and L. De Lorenzis. Stochastic phase-field modeling of brittle fracture: Computing multiple crack patterns and their probabilities. *Computer Methods in Applied Mechanics and Engineering*, 372:113353, 2020.
- [28] C. Goll, T. Wick, and W. Wollner. DOpElib: Differential equations and optimization environment; A goal oriented software library for solving pdes and optimization problems with pdes. *Archive of Numerical Software*, 5(2):1–14, 2017.
- [29] V. Hakim and A. Karma. Laws of crack motion and phase-field models of fracture. *J. Mech. Phys. Solids*, 57(2):342–368, 2009.
- [30] T. Heister, M. F. Wheeler, and T. Wick. A primal-dual active set method and predictor-corrector mesh adaptivity for computing fracture propagation using a phase-field approach. *Comp. Meth. Appl. Mech. Engrg.*, 290:466–495, 2015.
- [31] M. Hinze, R. Pinnau, M. Ulbrich, and S. Ulbrich. *Optimization with PDE Constraints*. Number 23 in Mathematical modelling: theory and applications. Springer, Dordrecht u.a., 2009.
- [32] D. Jodlbauer, U. Langer, and T. Wick. Matrix-free multigrid solvers for phase-field fracture problems. *Computer Methods in Applied Mechanics and Engineering*, 372:113431, 2020.

- [33] D. Jodlbauer, U. Langer, and T. Wick. Parallel matrix-free higher-order finite element solvers for phase-field fracture problems. *Mathematical and Computational Applications*, 25(3):40, 2020.
- [34] A. Karma, D. Kessler, and H. Levine. Phase-field model of mode iii dynamic fracture. *Physical Review Letters*, 87(4):45501–618, 2001.
- [35] D. Khimin, M. C. Steinbach, and T. Wick. Optimal control for phase-field fracture: Algorithmic concepts and computations. In F. Aldakheel, B. Hudobivnik, M. Soleimani, H. Wessels, C. Weïßenfels, and M. Marino, editors, *Current Trends and Open Problems in Computational Mechanics*. Springer, 2022.
- [36] A. Khodadadian, N. Noii, M. Parvizi, M. Abbaszadeh, T. Wick, and C. Heitzinger. A Bayesian estimation method for variational phase-field fracture problems. *Computational Mechanics*, 66:827–849, 2020.
- [37] D. Knees, R. Rossi, and C. Zanini. A vanishing viscosity approach to a rate-independent damage model. *Mathematical Models and Methods in Applied Sciences*, 23(04):565–616, 2013.
- [38] L. Kolditz and K. Mang. On the relation of gamma-convergence parameters for pressure-driven quasi-static phase-field fracture. *Examples and Counterexamples*, 2:100047, 2022.
- [39] A. Kopanicakova and R. Krause. A recursive multilevel trust region method with application to fully monolithic phase-field models of brittle fracture. *Computer Methods in Applied Mechanics and Engineering*, 360:112720, 2020.
- [40] C. Kuhn and R. Müller. A continuum phase field model for fracture. *Engineering Fracture Mechanics*, 77(18):3625 – 3634, 2010.
- [41] K. Mang, T. Wick, and W. Wollner. A phase-field model for fractures in nearly incompressible solids. *Computational Mechanics*, 65(1):61–78, 2020.
- [42] D. Meidner. *Adaptive Space-Time Finite Element Methods for Optimization Problems Governed by Nonlinear Parabolic Systems*. PhD thesis, University of Heidelberg, 2008.
- [43] A. Mesgarnejad, B. Bourdin, and M. Khonsari. Validation simulations for the variational approach to fracture. *Computer Methods in Applied Mechanics and Engineering*, 290:420 – 437, 2015.
- [44] C. Miehe, M. Hofacker, and F. Welschinger. A phase field model for rate-independent crack propagation: Robust algorithmic implementation based on operator splits. *Comput. Meth. Appl. Mech. Engrg.*, 199:2765–2778, 2010.
- [45] C. Miehe, F. Welschinger, and M. Hofacker. Thermodynamically consistent phase-field models of fracture: variational principles and multi-field fe implementations. *Int. J. Numer. Methods Engrg.*, 83:1273–1311, 2010.
- [46] F. Mignot. Contrôle dans les inéquations variationnelles elliptiques. *Journal of Functional Analysis*, 22(2):130–185, 1976.

- [47] F. Mignot and J. P. Puel. Optimal control in some variational inequalities. 22(3):466–476, May 1984.
- [48] A. Mikelić, M. Wheeler, and T. Wick. A phase-field approach to the fluid filled fracture surrounded by a poroelastic medium. ICES Report 13-15, Jun 2013.
- [49] A. Mikelić, M. F. Wheeler, and T. Wick. Phase-field modeling through iterative splitting of hydraulic fractures in a poroelastic medium. *GEM - International Journal on Geomathematics*, 10(1), Jan 2019.
- [50] M. Mohammadi and W. Wollner. Phase field modelling of fracture. *Optimization and Engineering*, 2020.
- [51] I. Neitzel, T. Wick, and W. Wollner. An optimal control problem governed by a regularized phase-field fracture propagation model. *SIAM Journal on Control and Optimization*, 55(4):2271–2288, 2017.
- [52] I. Neitzel, T. Wick, and W. Wollner. An optimal control problem governed by a regularized phase-field fracture propagation model. Part II: The regularization limit. *SIAM Journal on Control and Optimization*, 57(3):1672–1690, 2019.
- [53] N. Noii, A. Khodadadian, J. Ulloa, F. Aldakheel, T. Wick, S. Francois, and P. Wriggers. Bayesian inversion for unified ductile phase-field fracture. *Computational Mechanics*, 2021.
- [54] N. Noii, A. Khodadadian, and T. Wick. Bayesian inversion for anisotropic hydraulic phase-field fracture. *Computer Methods in Applied Mechanics and Engineering*, 386:114–118, 2021.
- [55] S. M. Robinson. Stability theory for systems of inequalities, part ii: Differentiable nonlinear systems. *SIAM Journal on Numerical Analysis*, 13(4):497–513, 1976.
- [56] R. Spatschek, E. Brener, and A. Karma. Phase field modeling of crack propagation. *Philosophical Magazine*, 91(1):75–95, 2011.
- [57] F. Tröltzsch. *Optimale Steuerung partieller Differentialgleichungen - Theorie, Verfahren und Anwendungen*. Vieweg und Teubner, Wiesbaden, 2nd edition, 2009.
- [58] J. Wambacq, J. Ulloa, G. Lombaert, and S. François. Interior-point methods for the phase-field approach to brittle and ductile fracture, 2020.
- [59] T. Wick. An error-oriented Newton/inexact augmented Lagrangian approach for fully monolithic phase-field fracture propagation. *SIAM Journal on Scientific Computing*, 39(4):B589–B617, 2017.
- [60] T. Wick. Modified Newton methods for solving fully monolithic phase-field quasi-static brittle fracture propagation. *Computer Methods in Applied Mechanics and Engineering*, 325:577–611, 2017.
- [61] T. Wick. *Multiphysics Phase-Field Fracture: Modeling, Adaptive Discretizations, and Solvers*. De Gruyter, Berlin, Boston, 2020.

- [62] B. J. Winkler. *Traglastuntersuchungen von unbewehrten und bewehrten Betonstrukturen auf der Grundlage eines objektiven Werkstoffgesetzes für Beton*. PhD thesis, Uni, 2001.
- [63] J.-Y. Wu, V. P. Nguyen, C. Thanh Nguyen, D. Sutula, S. Bordas, and S. Sinaie. Phase field modelling of fracture. *Advances in Applied Mechanics*, 53:1–183, 09 2020.
- [64] T. Wu, B. Rosic, L. de Lorenzis, and H. Matthies. Parameter identification for phase-field modeling of fracture: a Bayesian approach with sampling-free update. *Computational Mechanics*, 67:435–453, 2021.
- [65] A. Zehnder. *Fracture mechanics*. Springer-Verlag, 2012.
- [66] J. Zowe and S. Kurcyusz. Regularity and stability for the mathematical programming problem in banach spaces. *Applied Mathematics and Optimization*, 5(1):49–62, Mar. 1979.